EUROPEAN FUSION DEVELOPMENT AGREEMENT

EFDA–JET–PR(04)47

M.L. Walker, D.A. Humphreys, D. Mazon, D. Moreau,
M. Okabayashi, T.H. Osborne, E. Schuster, and JET EFDA Contributors

Emerging Applications in Tokamak Plasma Control

Emerging Applications in Tokamak Plasma Control

M.L. Walker[1], D.A. Humphreys[1], D. Mazon[2], D. Moreau[3],
M. Okabayashi[4], T.H. Osborne[1], E. Schuster[5], and JET EFDA Contributors*

[1]General Atomics, P.O. Box 85608, San Diego, California 92186-5608, USA
[2]EURATOM-CEA Association, DSM-DRFC, CEA-Cadarache, 13108 St Paul lez Durance, France
[3]EFDA-JET CSU, Culham Science Centre, Abingdon, OX14 3DB, United Kingdom
[4]Princeton Plasma Physics Laboratory, Princeton, New Jersey
[5]Lehigh University, Dept. of Mechanical Engineering and Mechanics, Bethlehem, Pennsylvania
** See annex of J. Pamela et al, "Overview of Recent JET Results and Future Perspectives", Fusion Energy 2002 (Proc.19 [th] IAEA Fusion Energy Conference, Lyon (2002)).*

Preprint of Paper to be submitted for publication in
IEEE Control Systems Magazine

1. INTRODUCTION

Many of the articles in this special issue focus on the problem of control of plasma axisymmetric shape and position. It is the best understood of tokamak control problems and, therefore, has the most results to discuss. There are also a large number of other tokamak control problems that are not nearly as mature in control development, but are equally important to continued progress toward the goal of producing energy from fusion. Work on these problems is active and growing rapidly. Areas of active development include work on basic physics understanding, developing actuators and sensors for control, development of control models including experiments to characterize actuators and sensors, experimental use of initial *ad hoc* controls, and development (and even a few deployments) of sophisticated control algorithms. In this article we provide a brief introduction to several of these control problems. For those problems that are discussed, we provide examples of progress that has been made at different tokamak devices around the world. In almost all cases we are unable, because of space considerations, to provide a complete accounting of all work on a particular class of control problems.

A practical tokamak fusion reactor must operate at high temperature, high pressure, and high current. These high performance tokamak plasmas are susceptible to a large number of instabilities, some of them posing a risk to the device itself. One example seen earlier in this issue is the so-called vertical instability due to noncircularity of the plasma. The vertical instability is axisymmetric, that is the plasma motion is the same at all toroidal angles, and is characterized by a primarily vertical displacement. Increases in growth rates of the vertical instability and of other plasma instabilities correspond to increases in plasma pressure. Consequently, the most attractive operational regimes from the point of view of a fusion power reactor also tend to be those that are nearest to instability.

Increasing temperature, pressure, and current cause several non-axisymmetric instabilities that must be stabilized. Most, but perhaps not all, will require feedback control. In this article, we will describe the control problems presented by instabilities known as resistive wall modes (RWM), neoclassical tearing modes (NTM), and edge localized modes (ELM). The objective of stabilization is to prevent loss of the plasma while retaining high performance; pushing the plasma into higher performance regimes is often what triggers a particular instability. Models upon which stabilization algorithms are based all start with ideal magnetohydrodynamic (MHD) theory (sidebar S3), but each requires an extension to that basic theory to correctly account for all important effects.

There is also a collection of control problems that might collectively be called control of internal plasma parameters: control of the current, temperature, and density profiles (sidebar S4), and control of transport (the continuous flow of particles, heat, and/or current) in the plasma interior. One particular combination of this class of problems will also be described.

There are also a number of *off-normal* events that can occur which must be “handled” rather than controlled in the sense of feedback. Off-normal events are events that are likely to occur due to occasional loss of control in future devices (and that routinely occur in present-day devices). A

description of several of these events will be provided. Efforts have been made on various experimental devices to define and implement appropriate responses to some types of off-normal events. A few of these methods will be described.

A GUIDE FOR THE READER (SIDEBAR)

This paper covers a number of separate tokamak control problems, each of which requires some background understanding of a variety of basic plasma physics topics. We rely heavily on the introductory paper and collection of numbered sidebars in this special issue to provide this background. In most cases, a reference to the introduction paper or appropriate sidebar is included when it is thought that a term or concept might be unfamiliar to some readers. For further assistance, at the end of the introduction paper there is a list of many plasma physics terms and the locations where each is defined. Each section of this paper discusses a completely separate control problem and all are written so that they can be read more or less independently of the other sections. The separate topics are ordered approximately in order of the level of physics background needed to understand them.

SUPPRESSION OF THE NEOCLASSICAL TEARING MODE

Increasing beta (sidebar S2) in a resistive plasma can make the nested magnetic surface topology required by ideal MHD (sidebar S3) unstable, resulting in a *tearing* and *reconnection* of the flux surfaces. When this reconnection occurs, a structure called a *magnetic island* is formed (Fig.1). The instability known as a *neoclassical tearing mode* (NTM) drives an island to a saturated size, which then persists stably in the plasma [1]. The island actually winds helically around the tokamak with a helicity given by the value of the factor q (sidebar S4) on the surface where it forms. The NTM forms on flux surfaces whose safety factor (q) is rational, the most important of which are the =3/2=1.5 or the =2/1=2.0 surfaces. The 2/1 NTM often produces a plasma-terminating disruption (sidebar S14) by triggering an ideal MHD mode, which can grow to be comparable in size to the plasma cross section, while the 3/2 NTM usually remains small enough to merely degrade confinement. The presence of the island can degrade confinement because it effectively connects hotter inner regions of the plasma more directly to colder outer regions with “short circuiting” magnetic field lines, allowing heat to leak out of the plasma core faster than it would without the island. The resulting flattening in temperature, pressure, and current profiles across the island (Fig.2) corresponds to a steady-state lowering of total plasma internal energy and therefore an overall colder, less efficient plasma.

S14. PLASMA DISRUPTIONS (SIDEBAR)

Disruptions are rapid events in which a large fraction of the plasma thermal energy is lost due to the uncontrolled growth of some large-scale plasma instability. These large-scale instabilities take place over a large portion of the plasma cross section. In most cases disruptions are unrecoverable, expelling

nearly 100% of the thermal energy and leading to complete termination of the plasma current. More rarely, disruptive instabilities can fail to expel all of the thermal energy and may even allow the discharge to recover (a *minor disruption*). Two broad classes of events account for the vast majority of plasma-terminating disruptions in tokamaks: major disruptions and vertical displacement events (VDEs). VDEs are unique to plasmas that are intrinsically unstable to vertical displacements (the *vertical instability*; see sidebar S6). This only exists in plasmas that are sufficiently vertically elongated (have cross sections that are higher than they are wide). A VDE is characterized by a loss of vertical position control, which allows the vertical instability to grow. The resulting vertical drift causes the plasma to strike a nearby surface, which erodes away the plasma as it continues to move into the wall. This erosion eventually destabilizes a large-scale instability, which expels all of the thermal energy. Following this *thermal quench* the plasma is always too cold and resistive for the ohmic transformer (sidebar S13) to sustain the plasma current, which decays away and terminates the plasma. By contrast, a major disruption is characterized by a sudden thermal quench triggered by a large-scale instability before any loss of position occurs. In this case the plasma becomes cold and resistive when more or less centered in the tokamak, and much of the plasma current can decay away before any subsequent loss of position causes the plasma to strike the wall.

Disruptions are undesirable in reactors due to a host of potentially damaging effects. The thermal quench can apply a large heat load to the first wall or divertor (sidebar S9), possibly melting protective surfaces. Large currents can be driven by the disruption in both plasma facing components and conducting structures, resulting in potentially damaging electromagnetic forces. The very high voltages produced in the cold post-thermal quench plasma can accelerate electrons into a relativistic beam. This million electron volt (MeV) scale electron beam can destroy many types of plasma facing components as the field lines they travel on intercept the first wall, much as an electron beam lithograph can etch features into semiconductor substrates.

Fortunately, many of these damaging disruption effects can be mitigated by taking corrective action as a stability limit is being approached, or even after the disruption is underway. Furthermore, understanding of the instabilities whose growth lead to disruptions has advanced to the point that many of these disruptive stability limits are predictable. However, it remains a challenge to be able to predict an impending disruption in real time early enough and with sufficient reliability to execute the necessary corrective or mitigating action.

In most cases, the NTM requires a triggering instability such as an ELM (see previous section) to produce a *seed island*, which will grow if the NTM is unstable [2]. One way of controlling the NTM is, therefore, to ensure that such triggering instabilities do not occur. Unfortunately, experimental evidence suggests that there are also seedless tearing modes, or NTMs triggered by background plasma turbulence, which is difficult or impossible to completely eliminate [3]. For this reason, relying on eliminating events that may produce a seed island may not be a sufficiently robust approach to NTM control. An alternate method for controlling NTMs using auxiliary current drive has been successfully demonstrated on several tokamaks. This approach replaces the current

lost in the process of flattening the profiles across the island, thereby shrinking the island, restoring the nested flux surface magnetic topology [Fig.1(a)], and stabilizing the mode [4]. As an alternative to this local control of the current profile (sidebar S5), global control of the current profile may also prevent NTMs. (See section on profile control.)

Current can be driven at the flux surface containing islands using a variety of methods. One method that can produce highly localized current drive and has been successful in stabilizing the NTM is electron cyclotron current drive (ECCD; see sidebar S13) [5]. This technique drives current in regions typically a few centimeters wide by injecting microwave frequency electromagnetic waves that resonate with the cyclotron orbits (Fig.9 of the intro article) of the current-carrying plasma electrons. In tokamaks such waves are typically produced by high power gyrotrons, similar to the wave generators used in satellite communications. The electron cyclotron frequency depends primarily on the toroidal magnetic field, so the current is driven where the injected wave path intersects the major radial location at which the waves are resonant. Figure3 illustrates this geometry in a DIII–D discharge. The injection chord is typically not straight owing to refractive effects of the plasma. For large tokamaks operating today (e.g., JET, DIII–D, ASDEX-U) injected power on the order of a few megawatts is required to produce the tens of kiloamps of plasma current needed to stabilize the mode [6]. Because islands are typically a few centimeters wide themselves, the alignment of island and deposition locations must be accomplished with accuracy on the order of a centimeter as well. The deposition need only lie on the flux surface containing the NTM islands, rather than directly threading the center of each helical island itself. However, actually driving current within each island (and not outside) would serve to reduce the power required to stabilize the mode.

S13. PLASMA HEATING AND CURRENT DRIVE

There are several methods in use at experimental devices for heating and driving current in the plasma. Those methods that have reached a maturity that makes them suitable for everyday experimental use include ohmic heating (OH) and current drive, neutral beam injection (NBI), and various forms of radio-frequency (RF) heating and current drive. All of these methods can actually accomplish both, but they are often configured with a primary purpose of either heating or current drive.

Ohmic current drive operates through a transformer action. Continuously changing current in one or more poloidal field coils produces a changing poloidal flux ψ, known as the *ohmic flux*, at the plasma. The derivative of this flux defines an induced voltage $V = d\psi/dt$ known as the plasma *loop voltage*, which drives current in the plasma according to $LdI/dt + RI = V$, just as in a standard transformer. Here the values L and R represent the plasma bulk equivalent self-inductance and resistance. Resistive losses in the plasma are responsible for the heating effect, hence the origin of the term *ohmic*.

Radio-frequency heating is a process by which electromagnetic waves are transmitted into the plasma and a portion of their energy is absorbed by the plasma. Wave energy is coupled to the

plasma particles primarily through resonant absorption. Resonant absorption occurs when the wave frequency is the same as a particle cyclotron frequency (see Fig.9 in the intro article), so that the wave's electric field increases the perpendicular velocity of the resonant particles. The direction of propagation of the RF waves determines whether this absorption results principally in heating the plasma or in a combination of heating and current drive. Wave propagation with a component parallel to the field lines can produce signficant current drive, while perpendicular acceleration principally produces heating. Typical ion cyclotron frequencies (ICH, ICCD) lie between 30 and 120Mhz, lower hybrid resonant frequencies (for a plasma mode that is a hybrid of electron and ion cyclotron motions) lie between 1 and 8GHz, and electron cyclotron resonant frequencies (ECH, ECCD) lie between 70 and 200GHz. Current can also be driven by coupling to fast magnetosonic waves (fast wave current drive, FWCD) or ion Bernstein waves (IBW) in the plasma [7].

Neutral beam injection (NBI) is the process by which neutral hydrogen or deuterium atoms are injected into the plasma at high speed, and then become ionized through collisions with plasma particles. The resulting ions and electrons then become part of the plasma. The kinetic energy carried by the originally neutral atoms is transferred to the plasma by both the initial and subsequent collisions, resulting in an increase in thermal energy (temperature) of the plasma. Because the high-energy beam ions collide primarily with the plasma thermal electrons, NBI can produce significant current drive when the beam is injected tangentially (i.e., in the toroidal direction). Tangentially injected neutrals also transfer their momentum to the plasma, thereby increasing the speed of plasma fluid rotation (see previous section on RWM). Perpendicular injection of neutral beams produces only heating.

Another interaction between heating and current drive is produced by the *resistivity* of the plasma. In the same way that resistance relates current and voltage in a resistor, resistivity relates local current density (electrical current flow per square meter of plasma cross section) to local electric field in the plasma. The resistivity varies in both spatial distribution and in time (at a given location). The change in resistivity is primarily determined by the local temperature, with increasing temperatures responsible for decreasing resistivity. Thus, (local) heating of the plasma will decrease the (local) resistivity, which in turn will tend to increase the (local) current flow. Thus, while NBI drives significant non-inductive current when injected tangentially, its primary effect is as a method of plasma heating, which has the collateral effect of broadening the current profile and increasing the plasma current for the same loop voltage. In a similar manner, electron cyclotron heating (ECH), when used for heating the plasma, can also have the effect of increasing the local current in the (highly localized) deposition region.

The timescale for ECCD-driven current to rise in a typical present-day tokamak is tens of milliseconds, comparable to the time required for the island to grow to a saturated state or to respond to the current drive and reduce in size (providing the deposition region is sufficiently well aligned with the island flux surface to produce suppression). Several mechanisms are available to perform the alignment on roughly this same timescale. One approach is to actively vary the wave launcher

mirror angle, which in turn varies the angle of the injection wave path (Fig.3) [5]. This has the advantage of leaving the plasma equilibrium characteristics unchanged. Another approach is to vary the toroidal field. This moves the major radial location of the harmonic resonance (and thus the deposition location) back and forth relative to the island (see Fig.3). This leaves the plasma shape and position unchanged, allowing divertor pumping (sidebar S9) and stability characteristics that depend on the shape to be held constant. This approach has been successfully used in stabilizing both 3/2 and 2/1 NTMs [8]. Still another approach involves movement of the plasma position (and thus the island position) relative to the approximately fixed deposition location. Moving the plasma radially can be accomplished with approximately fixed divertor pumping and plasma shape, but moving the plasma vertically tends to significantly affect the divertor configuration (although with little effect on the shape). Nevertheless, while modifying the toroidal field typically requires >100ms owing to the large L/R time of toroidal field coils, varying the plasma position requires <10ms. This speed advantage means that plasma position control can produce adequate alignment in a shorter time, and phase lags in the control action and island response are significantly reduced. Launcher angle control can, in principle, be comparable in speed to plasma position control.

The central problem in using these methods to align the current drive deposition and island locations arise from the difficulties in determining the location of the island flux surface and the deposition location in real time. Present-day diagnostics and equilibrium reconstructions produce estimates of the island flux surface location with typical accuracy of ±1 to 1.5cm, comparable to the control accuracy of the plasma position and toroidal field themselves. In addition, determination of the deposition location requires complex computation that at present cannot be accomplished in realtime. A suite of search and tracking algorithms has been developed on DIII–D to address these difficulties and produce successful, sustained NTM suppression. In particular, the DIII–D NTM control system makes use of three coupled algorithms: the Search and Suppress, Active Tracking, and Target Lock routines. Each of these can affect any of three different island/ECCD alignment control quantities: the plasma major radial position, the toroidal field, or the plasma vertical position. The operation mode that has been most successfully and routinely applied to date is a combined Search/Suppress and Active Tracking mode (Fig.4). When the control phase is enabled in this mode, the control algorithm fixes the selected control actuator quantity for a specified dwell time to determine whether the degree of alignment is sufficient to suppress the mode. If at the end of this dwell time the (filtered) mode amplitude has been reduced at a sufficiently high rate relative to a specified threshold rate, or has actually fallen below a specified threshold amplitude, the algorithm continues to hold the control quantity fixed. If the rate of suppression has not exceeded the threshold rate, the algorithm executes a search by incrementing the control quantity by a specified amount, freezing the control quantity for another dwell time, and examining the resulting effect on the mode. This search/dwell/search sequence continues until a specified limit is reached, and the search reverses the sign of the control quantity increment. This process continues until sufficient alignment is detected and the mode is suppressed below the specified amplitude threshold.

Once a sufficient alignment is detected, the control quantity is nominally frozen, and the Active Tracking algorithm is engaged. This algorithm adjusts the control quantity to maintain alignment in the absence of the mode. The required adjustment is determined by either a linear or nonlinear predictor calculation based on magnetic measurements, or on an explicit equilibrium reconstruction including measurement of the internal magnetic topology with motional Stark effect (MSE) sensors [9]. The MSE sensors measure the local ratio of poloidal and toroidal magnetic fields at many points within the plasma. Several predictors are available to the routine, including neural network-based algorithms. These are trained on previous experimental discharge data or artificially generated data to produce an estimate of the position of the relevant q-surface relative to the plasma geometric centroid. If toroidal field control is being used, the required toroidal field correction is derived from the predicted perturbation in the relative major radial position. While neural network predictors have been very successfully applied in DIII–D, flux surface reconstruction based on direct magnetic measurements has provided the most accurate and reliable sustained alignment in recent experimental campaigns.

Design of the parameters governing the Search and Suppress and Active Tracking algorithms was accomplished using accurate, experimentally validated dynamic models of NTM island response to ECCD and plasma response to position commands. Figure 4 shows a comparison of a mode suppression model and the experimental response to variation in the degree of alignment between island and ECCD location (top frame). The model response, based on a simplified version of the modified Rutherford equation that describes island dynamics, shows sufficiently accurate representation of island response dynamics to allow for good control design [3]. In the case shown, the plasma major radius (middle frame) was varied to adjust the alignment of the $q = 1.5$ surface with the ECCD deposition location. The NTM control algorithm is also integrated with a special plasma shape/position regulation scheme that fixes the strike points (Fig.14 of the intro article) while varying the major radius to adjust the island/ECCD alignment. This allows for constant divertor pumping (sidebar S9) while NTM suppression is performed. Following suppression of the mode, where it is assumed that deposition is aligned with the $q = 3/2$ surface, the Active Tracking algorithm is enabled to compensate for variations in the $q = 1.5$ surface due to changes in the current profile and poloidal beta. The Active Tracking action can be seen in the fluctuating major radius perturbations following suppression at $t \approx 3.4$s.

Figure 4 also summarizes experimental results from use of the Search and Suppress with Active Tracking. The growth of the mode is slowed even when the island and ECCD are misaligned by as much as 1.5 to 2cm. Adjustment of the major radius by the Search and Suppress produces sufficient alignment to fully suppress the mode within 200ms. After design and testing of the basic scheme, proper functioning of the algorithm requires specification of various parameters and thresholds to match the dynamic characteristics of the target equilibrium. Dynamic models of NTM response were sufficiently reliable that control system parameters designed using these models produced successful suppression and tracking of the evolution of the profile to maintain island/ECCD alignment

the first time this integrated active suppression was attempted experimentally.

An alternative to the Search/Suppress algorithm is the Target Lock algorithm. This control scheme uses the observed response of the mode amplitude to either natural fluctuations or preprogrammed variations in the control quantity to infer the proximity to ideal alignment. An approximate form of the modified Rutherford equation is implemented in this algorithm to provide an estimate of the expected mode decay or growth rate based on the degree of misalignment.

Use of Search and Suppress, Active Tracking, and Target Lock algorithms has enabled full and sustained suppression of both 3/2 and 2/1 NTMs in DIII–D under closed loop control without previous experimental determination of the ideal alignment location. Suppression of the 3/2 NTM has allowed operation at normalized beta values approximately 50% above the value achieved in the presence of the unsuppressed mode (from $\beta_N = 2.3$ to $\beta_N = 3.4$) [3]. The duration of increased-beta operation is presently limited only by the length of time that the gyrotrons can inject power into the plasma.

Eventual application of NTM suppression to fusion reactors envisions several possible modes of operation. In one scenario, current drive will be applied in steady state at the relevant flux surfaces to pre-emptively suppress any seed islands that may be triggered by background MHD instabilities or turbulence. Because the current drive source would have to operate constantly in this scenario, this would require a large amount of auxiliary power. This approach would also require constant tracking of the deposition location and target flux surfaces to maintain alignment. Another approach is to detect the presence of NTM islands and enable a suppression system to suppress the mode as rapidly as possible, hopefully before a 2/1 island reaches a potentially disruptive saturated size, or a 3/2 island significantly degrades confinement. This demands a very rapid island acquisition and alignment system to achieve suppression within tens of milliseconds after the onset of island growth. Of course, constant and accurate determination of the flux surface geometry and computation of the expected deposition location would allow the system to be engaged very quickly and could meet this suppression time requirement. Gyrotrons, for example, can be ramped to full power in significantly less than 10ms.

FUTURE DIRECTIONS

It is now widely accepted that localized current drive can replace the missing bootstrap current that characterizes the NTM, thereby stabilizing the mode. Several closed loop feedback approaches have demonstrated NTM suppression sustained for several seconds on various tokamaks. However, before current drive suppression can be used effectively in a reactor-grade plasma, several key capabilities must be demonstrated. The principal requirement in a reactor is reliable, simultaneous, and steady state suppression of both the 3/2 mode (which mainly degrades confinement) and the 2/1 mode (which can lead to a disruption). Such a demonstration will require more installed current drive power than any machine presently has, independently steerable launchers, more accurate and reliable realtime reconstruction of internal magnetic surfaces, accurate realtime determination of

the current deposition location, and algorithms that can deal with changing equilibrium and machine conditions. Work has begun on installing steerable launchers in several devices, and realtime steering has been demonstrated in JT–60U. Realtime magnetic surface reconstruction has been demonstrated in DIII–D, but present levels of noise and accuracy have limited the effectiveness of suppression over long periods. Algorithms for detecting the location of optimal alignment and maintaining alignment once the mode is suppressed have been developed, but leave much room for improvement. The field of NTM suppression in tokamaks is rapidly evolving, but would benefit greatly from contributions in the areas of improved control algorithms and approaches, estimation, realtime computation, actuator technology, and diagnostic signal interpretation.

DETECTION, CORRECTION, AND MITIGATION OF OFF-NORMAL EVENTS

An off-normal event is any event that would not normally occur during well-controlled routine steady state operation. There are a large number of such events, some examples of which will be described in this section. The impact of off-normal events in a tokamak can be summarized according to the severity of their consequences:

1. Risk of Personnel Safety. These are events that have the potential to cause harm to operating personnel or to the general public. A categorization of off-normal events from a safety point of view is given in [10].
2. Risk of Equipment Safety. These are events that have the potential to cause damage to either the device or the facility, but do not risk the safety of personnel.
3. Performance Degradation. These are events that can cause performance of tokamak operation to degrade, but do not create risk to either personnel or equipment.

The primary personnel risks at a tokamak facility are due to the high currents and voltages used in confining and heating the plasma, radiation from activated materials or tritium release, and conventional process control risks such as use of toxic chemicals and systems under pressure or with extremely high or low temperatures. Most of the approaches for dealing with these risks are rather conventional and are already in use at the major facilities, so will not be discussed in this section. The highest risks to the device or facility derive primarily from the large energy content in the plasma while the tokamak is operating. Off-normal events that lead to plasma termination such as major disruptions (sidebar S14) can deposit a significant amount of this energy onto plasma facing components (PFC) or create large and potentially damaging mechanical forces.

The handling of off-normal events represents another highly coupled category of control in tokamaks, and includes detection and identification of the off-normal event, determination and execution of corrective action when possible, and execution of a mitigating response when correction or recovery is not possible. In future power producing reactors, the system responsible for off-normal event detection and response must be thoroughly integrated with many other control subsystems in order to provide effective and appropriate action coordinated with other plasma control responses. Such responses must also be well-integrated with the overall safety and supervisory system.

Responses to off-normal events generally depend on the risk associated with the event. A *fast plasma termination* would usually be initiated if an event poses an imminent threat to personnel or to the device or facility. A fast plasma termination can cause structural damage by localized deposition of thermal or magnetic energy, however. To mitigate these effects, termination techniques that distribute the plasma energy more homogeneously are necessary. A *controlled plasma termination* is typically initiated when continued operation could lead to a potential risk situation. In present devices, discharges are typically not terminated for reasons of reduced performance, although this may not be the case with future devices. Usually, efforts are made to recover from the performance reducing event, either in the same discharge or in those that follow.

A fast plasma termination is not always the result of a controlled safety procedure. Sometimes it is the consequence of a control failure. This loss of controllability originates either in the failure of a component or subsystem of the feedback loop, or in the operation of the system at operating points for which the controller was not designed or at operating conditions that trigger other types of instabilities.

In the following sections, we provide descriptions of some methods for handling disruptions, system fault detection and isolation, and performance optimization. These are only a few examples of a much broader collection of problems that must be solved to enable a viable power producing fusion reactor.

DISRUPTION AVOIDANCE AND MITIGATION

Erosion due to disruption may consume a high percentage of the designed plasma facing components (PFC) lifetime. Sometimes, long-term reconditioning of plasma-facing surfaces after disruptions will be required before normal plasma operation can be resumed. It is desirable to avoid the occurrence of disruptions whenever possible and to reduce the direct and consequential effects of such disruptions. The approaches to disruption avoidance can be divided into two categories [11]: (1) a priori avoidance of the operation conditions that lead to disruption, and (2) active intervention in a discharge scenario after early prediction of disruption onset.

Disruptions can in principle, be avoided during tokamak operation by the use of a *disruption-free* scenario (sidebar S18) that avoids the various operational limits and conditions that cause disruptions, and by the provision of adequately reliable plasma operation and control systems such that all critical parameters of the prescribed scenario can be reliably obtained and repeated. However, optimizing plasma performance often requires operating near disruption limits.

Disruption-free scenarios are often based upon conservative plasma operation parameters that do not press close to known disruption-initiating limits or plasma control limits. A priori disruption avoidance procedures can in principle be extended to operation scenarios that come closer to several operational limits. In these cases, observation of the limits involved and provision of real-time disruption prediction or onset warning capability become important. Using a warning indicator of a potentially impending onset of disruption to effect feedback controlled intervention can lead to

reliable operation near a limit that can initiate disruption. Basing disruption prediction on single parameter proximity or the confluence of several single parameter limits may not necessarily provide complete certainty for disruption avoidance, or conversely, may unduly restrict the accessible operation domain. A possible improvement can be made by implementation of a neural network disruption predictor, wherein multiple disruption-related indicators or diagnostic signals are combined via a neural network to provide a composite impending disruption warning indicator that is more robust and reliable than simple single- or multiple-parameter indicators. For example, after training, neural networks were able to successfully predict disruptions in DIII–D [12] and classify disruptions in JET [13]. Enhanced predicting capabilities (85%) were also achieved in ASDEX-U using a neural network disruption predictor [14]. More complex systems [15]–are capable of disruption prediction with a probability of 95%.

Ideally, an impending disruptive MHD instability would be detected and avoided by modifying the target equilibrium, heating, density, or other operating parameters. Should such avoidance not be possible, mitigation of its effects is required. PFC damage is primarily due to an excessive surface temperature rise leading to melting or ablation, and this situation cannot be ameliorated through improved heat removal capability on the PFC heat sink. Effective thermal mitigation approaches involve maximizing the time over which the energy is released or expanding as much as possible the region over which the energy is deposited. This goal can be achieved by the fast injection of impurities. UV line radiation from the injected impurities distributes the plasma energy more uniformly on the first wall, reducing the thermal load to the divertor (sidebar S9). The most effective injection methods are solid pellet injection [16] and intense gas puffing [17].

FAULT DETECTION AND ISOLATION

During operation of a tokamak, hundreds of subsystems must operate correctly and simultaneously for a completely successful plasma discharge. On many devices, verifying proper operation of the subsystems most prone to failure is done manually by human operators after the discharge. Because of the tedious nature of this task and the large number of systems, inoperative or malfunctioning systems can sometimes remain undetected until several experimental discharges have passed. Occasionally, problems will not be detected until days later if the failure does not prevent operation. Due to the increasing complexity of tokamak experimental devices, some efforts have been made toward development of automated fault detection systems.

Fault detection and isolation (FDI) techniques have been under development for the last three decades. In the course of this development an FDI approach based on analytical redundancy has emerged in place of the more traditional FDI approach based on hardware redundancy [18]. In the latter approach, redundant physical subsystems (multiple sensors, for example) are built and their output signals are compared for consistency. In the event of failure, a subsystem backup is switched in. Higher costs, additional space requirements, and complexity make this approach often unattractive. In the former approach, the inherent redundancy contained in the static and dynamic relationships

among the inputs and outputs of the system is exploited for fault detection and isolation. The measurements of the system inputs and outputs are processed analytically to estimate the value of a desired variable. This estimate can be generated using either quantitative or qualitative models. For quantitative (mathematical) models, the model-based predictors are state estimation, parameter identification, and parity space. For qualitative (non-mathematical) models, the prediction is based on decision-table-based methods, knowledge-based expert systems, and neural-network-based methods. The estimated variable is then compared with the measured value of the variable to generate a residual. Deviation of this residual from the normal behavior significant enough to indicate a failure must then be detected by methods of change detection such as Bayes decision and hypothesis testing. Each type of fault is characterized by a specific combination of symptoms. Classification methods such as fuzzy clustering, artificial neural networks, and geometrical distance are used to determine the type of fault [19]. If more information about the relations between symptoms and faults is available in the form of diagnostic models, methods of reasoning can be applied. The reasoning strategies for fault diagnosis are probabilistic reasoning, rule-based reasoning, sign directed graph, fault symptom tree, and fuzzy logic. Due to the complexity of tokamak systems and the large number of variables to be monitored, current efforts toward fault detection and isolation in tokamaks are based primarily on qualitative approaches.

At JET, an automatic modular sensor fault detection and classification (SFDC) [20] system has been built for the sensors measuring the vertical mechanical stresses on the supports of the vacuum vessel of the tokamak. Experts are interested in the reliability of these measurements during specific time windows, corresponding to the occurrence of disruptions. During the usual operational life of the tokamak, in fact, mechanical stresses are weak and do not need to be monitored. During a disruption, on the contrary, fast dynamic vertical displacement events (VDEs) (sidebar S14) occur, causing an impulsive force and mechanical oscillations of the vacuum vessel, which must be monitored to assure the mechanical integrity of the machine. One of the actions related to the mechanical monitoring of the stresses is to suspend the experimental campaign when more than a fixed number of VDEs trespassing a certain stress threshold occurs in a day. The reliability of the measurements is therefore very important to avoid both unmotivated suspension of the experiments and dangerous experiments carried out above the operational limits. The strategy used is based on a modular system that consists of two stages. The first stage consists of a multilayer perceptron (MLP) neural network that has been trained to predict some features of the considered signals on the basis of a selected set of inputs [21]. The predicted features provided by the neural model can be compared with the actual feature values, in order to raise alarms indicating sensor faults if the corresponding residuals are too high. This task is part of the fault detection phase, which consists of revealing the presence of a fault. The second stage focuses on fault classification, which is accomplished by a fuzzy inference system (FIS). In this case, the fault classification rules were established on the basis of manual fault classification previously performed by experts. The tuning of the membership functions was set by trial and error, taking sensor accuracy and disturbance

level into account. As mentioned above, validation of stress measurements is only relevant during disruptions. The occurrence of a disruption is notified by a suitable flag provided by an automatic disruption detection tool already in existence at JET. It is possible, in this way, to select the experiments in which the sensor validation should be performed.

At present, an expert-system-based fault detection system is used routinely during DIII–D operations and has led to an increase in tokamak productivity. The Fault Identification and Communication System (FICS) [22] executes automatically after every plasma discharge to check dozens of device subsystems for proper operation and to communicate the test results to the tokamak operator. The primary purposes of FICS are fault detection and fault prediction. Fault detection refers to determining which systems were not working properly during an experiment, even if they do not cause the loss of the experimental discharge (shot). Fault prediction refers to determining which systems look like they are having trouble and may cause a future fault. This includes detecting programming errors, that is, determining whether the operator specified setup for a shot is self-consistent. The core of FICS uses the public domain software package called CLIPS (C language integrated production system), originally developed by NASA [23]. CLIPS, a computer language designed for implementing expert systems, provides two powerful capabilities not provided by conventional programming languages. *Chaining* provides the ability to emulate a human chain of reasoning in software. *Data driven* execution enables the expert defined rules to activate as soon as a knowledge or data source becomes available. The CLIPS shell performs the inferences, executing rules of the form “if A, then B”. CLIPS in its simplest form consists of facts and rules. Rules are executed when specified facts are asserted (A in the clause”“if A, then B”). The consequences of a rule execution are to assert other facts (B), which can then execute other rules, and so on. A very important side effect of rule execution is the ability to activate functions that extract and manipulate data and return the results of those manipulations to the expert system. This information can then also be used to assert more facts to drive other rules, and so on. The order of rule execution can be influenced by a priority value assigned to each rule. Rules are executed according to their relative priority and according to when their data becomes available. Since the program is data driven, each rule executes if and when the data shows up. If a particular piece of data is not available, tests that require that data do not execute and an alarm is raised saying the needed data was not acquired.

The success of any fault detection system is linked to the availability of adequate measured data. Present devices already acquire a huge amount of experimental data, sometimes several Gigabytes per discharge of only a few seconds duration. Steady state operation will put significant demands on data storage, even with relatively slow rates of data acquisition. On the other hand, the data acquisition system must be able to capture rapid and unpredictable changes for use in fault detection and identification. For this purpose, new data acquisition methods were developed for the TRIAM–1M [24] and JET [25] tokamaks in order to combine coarse data from quiescent steady-state phases with fine data from rapid and unpredictable transitions.

PERFORMANCE OPTIMIZATION THROUGH EVENT HANDLING

Catastrophic loss of plasma or failure of tokamak systems are the most obvious off-normal events. Other events are more subtle in that they simply degrade performance. Thus methods to handle and correct these events can be thought of as performance optimization. A good example of this is the detection and handling of the H–mode to L–mode back-transition (sidebar S11) that occurs in ASDEX-U [26]. The performance control in ASDEX-U is dedicated to the control of plasma characteristics like confinement or radiative behavior, which can be relatively well separated from those related to the plasma position and shape control. Several process controllers, usually simple single-variable PI controllers, have been implemented to control different characteristics of the plasma such as various forms of density, temperature, and pressure as well as fueling mixtures and power flows. These basic process controllers are combined to define so-called control recipes that are switched on and off during the discharge. Activation of the control recipes at preset times during the discharge to optimize some plasma characteristic is not practical because it is difficult, if not impossible, to predict the conditions of the plasma. A real-time algorithm for plasma regime recognition was therefore developed to be used as the trigger mechanism for the control recipes. The first version implemented identifies five different confinement regimes (sidebar S11): Ohmic Phase (OH), standard L–Mode (L), standard H–Mode (H), highly radiating L–Mode (HRL), highly radiating H–mode (HRH). This algorithm allows the switching of control recipes to recover plasma performance. For example, the working point for best HRH plasma performance is close to the H–mode to L–Mode back transition, so occasional back transitions occur. When they do, the regime recognition algorithm is used to dynamically switch to another control recipe to restore the desired HRH mode.

FUTURE DIRECTIONS

Methods for ensuring personnel safety have been largely systematized in existing tokamak devices. Anticipated new dangers in next generation devices include the use of larger amounts of radioactive tritium, greater neutron production within the device, and the resulting neutron activated plasma facing materials. It is not expected that this will present any major difficulties because new facilities will be able to draw on many decades of nuclear industry experience. In addition, various types of loss of cryogenic (for superconducting coils) coolant accidents are envisioned that may or may not present a danger to personnel, but will certainly endanger the device.

A number of new methods will be needed to deal with other types of off-normal events. Many of the present methods of fault detection and diagnosis for these events execute primarily off-line and between plasma pulses. These methods will need to be converted to on-line detection algorithms when steady state devices are put into use. A great deal of the required knowledge for how to detect faulty tokamak systems now resides only in the minds of experienced operators. This knowledge will need to be captured and models of various tokamak support systems will need to be developed in order to incorporate them into on-line fault diagnosis software. Present day devices typically do

not maintain the functional models of tokamak support systems that would be necessary for fault detection.

For those faults that can lead to device safety issues, methods for controlled shutdown of the plasma pulse must be further developed and must be expanded to include a greater number of faults. In particular, reliable and safe on-line methods for remediation of large energy events must be implemented and proven. For example, mitigation of plasma disruptions through massive gas puffing is now being implemented and tested on several experimental devices but, even at DIII–D where these methods were pioneered, they are not yet a part of routine operation.

EDGE LOCALIZED MODES

A defining feature of high energy confinement (H–mode; see sidebar S11) tokamak plasmas is the existence of a region of significantly reduced thermal and particle diffusion near the plasma boundary, called the–*edge transport barrier* or ETB (sidebar S12). Although the high performance of H–mode plasmas results from high pedestal temperatures and densities (Fig.6) obtainable with an ETB, the very low transport in the edge region generally leads to a rise in the gradient of the pressure distribution near the edge, which triggers an instability localized to the plasma edge known as the *edge localized mode* (ELM) [27].

S11. CONFINEMENT MODES (SIDEBAR)

The *energy confinement time*, τ_E (sidebar S2), is an important measure of the ability of a plasma to retain energy and thereby support continuing fusion reactions. In the tokamak experimental community, plasmas are typically categorized as one of four different *confinement modes* when describing their confinement properties. The first of these is the ohmic plasma, which is heated only by the ohmic transformer action (sidebar S13). The three remaining modes all use methods of auxiliary heating as well as ohmic heating. In order of increased confinement, these are the *low confinement mode* or *L–mode*, the *high confinement mode* or *H–mode*, and several versions of very high confinement modes. These modes are primarily distinguished by the shape of their temperature, pressure, and density profiles (sidebar S5) with the higher confinement modes exhibiting steeper gradients there. The terms ohmic plasma, L–mode, and H–mode have become more or less accepted terminology, while the term describing the highest confinement regime varies between institutions. Even though higher confinement regimes have been identified, H–mode [28] is the target regime for the advanced tokamak (AT) concept, because the higher confinement modes have only been produced transiently, always being terminated by a severe MHD instability. The AT requirement for active control has driven much of the recent research in methods of control for tokamak quantities.

S12. EDGE TRANSPORT BARRIERS (SIDEBAR)

Discussion of the ELM instability centers on transport and MHD behavior in the *edge transport barrier* of the plasma (Fig.5). In contrast to global modes such as the RWM (see second section of

this article), the ELM is primarily localized to this edge region. The height of the temperature pedestal (Fig.5) acts almost as a multiplier for temperatures inside the plasma. The greater the pedestal height the greater the total energy content of the plasma. Inside the knee, the temperature is approximately 10 times that of the sun's center (1000eV), while exterior to the plasma it is about 10eV. The source of the ELM instability is the resulting large pressure gradient in the edge region. During an instability, a significant amount of the pedestal energy (up to 25%) can leave the plasma and be deposited on plasma facing components.

ELMs are most often observed as bursts of light (measured using photodiodes) from excited hydrogen or deuterium atoms [Fig.7(a)] in regions where the ELM power flux reaches the vessel wall. The magnetohydrodynamic instability that is believed to be responsible for the larger type of ELMs in Fig.7(c) perturbs the magnetic field and can also be observed on magnetic probes mounted on the vessel wall [Fig.8(b)].

The physics processes of the ELM are not completely understood although significant progress has been made. Theories based on ideal MHD (sidebar S3) seem to be in good agreement with the early linear phases of the mode growth. The later nonlinear growth of the mode is an active area of research. Figure 9 shows the mode structure in the nonlinear growth phase as predicted by one proposed model [30]. This figure is consistent with the intuitive picture of ELMs — the nested flux surfaces characterizing ideal MHD are broken by the instability and, consequently, particles and heat can be removed through the plasma edge.

The three ELM types that are observed in most tokamaks [27] are summarized in Table1. They are experimentally distinguished by the dependence of the ELM frequency on heating power, (Fig.7), the density of the plasma, and the shaping applied to the plasma cross section.

Each ELM causes a collapse of the ETB and can cause a loss on the order of 5% of total plasma stored energy on a very short time scale. Although the ETB forms again following the ELM and the energy confinement of H–mode discharges with ELMs is still much superior to discharges with no ETB, the very large power loss during the ELM (in a tokamak reactor this is projected to be tens of gigawatts) creates severe difficulties in the design of the tokamak power exhaust handling structures (Fig.10). Work on ELMs has therefore focused on developing techniques for either (1) reducing the ELM power loss (either by reducing the total ELM energy loss or extending the time over which the energy is lost), or (2) enhancing the particle transport in the ETB or possibly raising the ELM instability threshold, to keep the pressure gradient below the critical level that triggers the ELM. However these approaches must also maintain a high quality ETB for good overall confinement.

The second of the two ELM control techniques above would seem to be solved by operating with the so called "ELM-free" discharges sometimes produced in tokamaks. In ELM-free discharges, the plasma has a high critical (threshold) pressure gradient for the ELM instability and input power is kept sufficiently low that this critical pressure gradient is not reached. However this results in another difficulty. Impurities are continuously produced by plasma interaction with device

components that face the plasma or as products of fusion reactions. Impurities entering the plasma edge are generally ionized in or near the ETB. They are then transported inward to the plasma core (by diffusion and by another mechanism that will not be discussed here) where they strongly interfere with fusion power production. ELMs act to reduce the source of these impurities by removing them periodically in their region of ionization. Thus ELM-free discharges typically exhibit impurity accumulation and are not considered to be viable solutions. Any technique that solves the ELM problem by eliminating the ELMs must also provide an alternate mechanism for reducing the impurities in the plasma. In addition to impurity removal, ELMs provide a mechanism for density control. If ELMs are eliminated, an alternate method for density control is also needed.

EXPERIMENTAL APPROACHES TO CONTROL

Several promising approaches for reducing or eliminating ELMs have been explored, but none yet presents a clear solution path. An ideal method would provide transport of particles out of the plasma, but without the associated transport of heat that degrades confinement. None of the currently proposed control methods involves feedback.

Several experiments have shown that regular injection of deuterium fuel or impurities in the form of frozen gas pellets or by gas puffing can trigger ELMs and/or change their characteristics. For example, experiments at the ASDEX-Upgrade (ASDEX-U) tokamak [31] have shown that repetitive deuterium pellet injection can trigger more frequent, smaller ELMs. Energy losses are thus spread over longer times, with smaller peak losses. There is some resulting loss of confinement, but not as severe as with naturally occurring ELMs. Using this method, only ELMs initiated by pellets occur. Gas fueling has also been shown to produce ELMs of smaller size. In cases where the Type I ELM size is reduced with increased gas fueling, the reduced ELM size is believed to be caused by a narrowing of the steep pressure gradient region near the separatrix relative to the ETB width (see Fig.5). (The narrower pressure gradient region enables instabilities to be triggered more easily, allowing less time for energy to build up between ELMs.) In present experiments this effect also results in reduced core stored energy. However, in a reactor scale tokamak, it is speculated that a confluence of factors enabled by the expected much higher pedestal temperature may mitigate this reduction in performance.

One class of experiments has shown that Type I ELMs can be converted to Type II or III by means of oscillation of the plasma position. At TCV [32], vertical position oscillations of a few millimeters induced higher frequency ELMs, some apparently locking to the oscillation frequency. If this is done on a frequency greater than the natural ELM frequency, the ELM size is reduced. The cause of the ELM triggering is unclear at present although it is speculated that the vertical motion induces current in the plasma edge triggering the instability. It is unknown whether this technique will be compatible with good performance in a reactor scale tokamak.

Experimentalists at the Alcator C–Mod tokamak have discovered an ELM-free H–mode regime called enhanced D-alpha (EDA) [33] having enhanced particle transport without an accompanying

increased energy transport. This regime is characterized by the presence of high frequency (>100kHz) fluctuations in the edge that seem to provide the necessary mechanism for enhanced particle transport for density control and for removal of impurities. The EDA has the desired characteristics, but other devices have so far been unable to reproduce it (except, perhaps, for the JFT-2M tokamak in Japan [34]). In addition, the continuous edge instability is thought to be associated with high edge resistivity (sidebar S13) and thus may not occur in a reactor scale tokamak.

Experiments at DIII–D have demonstrated a new regime known as Quiescent H–mode (QH–mode) [35] that allows ELM-free operation, with a key feature being the presence of an edge electromagnetic oscillation known as the edge harmonic oscillation (EHO) [36]. The EHO enhances the particle transport through the edge without significantly increasing the thermal transport. The QH–mode operation has also been demonstrated at ASDEX-U [37] and QH–mode periods have been seen in discharges in JET and JT60–U. Although QH–mode occurs in a more reactor-relevant regime than EDA, it appears to require some level of toroidal rotation of the edge plasma in the direction opposite to the direction of the plasma current. The physics of the QH–mode is not understood presently and its applicability to a reactor scale tokamak is unclear.

Evans, et al. [38] has demonstrated a method for suppression of large ELMs in high confinement plasmas by creating a *stochastic magnetic boundary*. A stochastic boundary refers to a randomization of magnetic flux contours at the plasma edge in place of the nested contours characteristic of ideal MHD (sidebar S3). Experiments at DIII–D and subsequent analysis show that imposition of a non-axisymmetric field can randomize the flux at the plasma edge and provide a means for steady state transport of particles out of the plasma, in contrast to the impulsive transport of ELMs. ELMs are reduced or eliminated while maintaining a high H–mode pedestal (Fig.5). Present stochastic boundary experiments used steady state non-axisymmetric magnetic perturbations, which have the side effect of slowing plasma rotation, and could result in destabilizating the RWM instability. (See section on stabilization of the RWM.) Proposed methods would use an oscillating field perturbation, which may not have this problem. This approach is promising for ITER, because it is practical to implement, but the physics is not well understood yet. Although the method was successful in experiments with an ITER shape scaled to fit the DIII–D vacuum vessel, extrapolation to the complete set of ITER plasma parameters has not yet been shown.

FUTURE DIRECTIONS

An H–mode regime with Type I ELMs has been chosen as the standard operating scenario (sidebar S18) for ITER [39] because it is capable of being sustained in steady state with high confinement. On-going investigations of ELMs have focused on evaluating the adequacy of this choice as well as considering possible alternatives in the event that this choice proves inadequate. These alternatives consist of both modified operating regimes that avoid Type I ELMs and open loop methods to alter the character of the ELM instability. It is a bit premature to discuss issues of feedback control for ELMs, since the physics mechanisms are not well understood yet. However, there are often precursors

to ELM events, sometimes several milliseconds long. This suggests the possibility that such precursors might be used to preempt or to mitigate the ELMs. This has not been done so far because the complicated and variable mode structure and high growth rates (10μs) for the instability in the case of Type I ELMs present a very challenging control problem. The question remains whether a feedback control strategy would be feasible once the mode and its precursors were better understood.

STABILIZATION OF RESISTIVE WALL MODES

In this section, we discuss one of the major tokamak non-axisymmetric instabilities — the resistive wall mode (RWM). The RWM is a form of plasma *kink instability* under the influence of a resistive wall. The word kink is very appropriate to characterize the RWM behavior, which is similar to a garden hose kinking when it is suddenly pressurized (Fig.11). The entire plasma configuration deforms in a helically symmetric manner. The toroidal mode number n (sidebar S4) is used to identify the helicity of the deformation. For RWM control, we are primarily interested in the lowest mode number n = 1 since the n = 1 instability is the first to occur with rising pressure. The achievable plasma pressure in power reactors is expected to be limited by the n = 1 mode, but it is predicted that the n = 2 mode will also go unstable if the n = 1 mode is stabilized and the pressure continues to rise.

When the plasma undergoes a non-axisymmetric distortion as in Fig.11, the current flowing in the plasma moves with it. Thus the magnetic flux and field that this current generates also moves with the fluid disortion. This moving magnetic field induces eddy currents in the surrounding conductive structures similar to the way in which eddy currents are induced by the vertical instability (sidebar S17). These induced currents, in turn, generate magnetic fields that oppose the plasma deformation, as in the case of the vertical instability. The overall effect of the presence of a conducting wall is to transform a plasma deformation with an extremely fast growth time (a few microseconds) into a combined plasma/wall system with an instability having a growth time on the order of the resistive decay time of eddy currents in the surrounding materials (a few milliseconds). This slower growth enables use of feedback to control the RWM instability.

The magnetic field motion due to the plasma fluid deformation is observable outside the plasma by magnetic sensors. Even though the deformation of the plasma surface cannot be directly measured in real time, the magnitude and direction of the deformation can be inferred from the external magnetic sensor measurements (Fig.12). Magnetic sensors are structurally simple and robust so they serve as the best sensors for a magnetic feedback control approach. Other, non-realtime diagnostics are used for developing understanding and modeling of the physical processes. Examples of the diagnostic measurements used in RWM analysis are shown in Fig.13.

THE PHYSICS OF THE RWM

According to MHD theory, a sufficiently high plasma pressure makes the RWM unstable when the surrounding wall structure is located far from the plasma surface. The plasma pressure threshold

for this instability is expressed in terms of a critical value of normalized beta β_N (sidebar S2). The unstable eigenmode could, in theory, be completely stabilized by the mode-induced eddy currents in the wall if the plasma were surrounded by a perfectly conducting wall within a critical distance. [A perfect conductor is a conductor without resistance, implying that there is no resistive decay of the stabilizing eddy currents induced by the eigenmode (sidebar S17).] In actual devices, the wall current decays away due to resistive losses and the mode amplitude grows with a growth time that is a fraction of the wall time constant. The critical value of beta for which the plasma becomes unstable without a perfectly conducting wall is called the *no wall beta limit*. With a further increase of plasma pressure, the RWM would become unstable even in the presence of a perfectly conducting wall. The value of beta for which this happens is called the *ideal wall beta limit*.

Ideal MHD gives a detailed prediction of the structure of the RWM as illustrated in Fig.14. MHD also predicts that the RWM amplitude is larger at the outer major radius side of the plasma (see Fig.12 of the intro article) than at the inboard side. This is due to the nature of the confining toroidal field, which decreases away from the torus axis of symmetry (the Z axis in Fig.12 of the intro article) so that the magnetic field pressure is relatively weaker at the outer major radius. This leads to the RWM perturbation amplitude being larger at the outer edge of the plasma. This suggests that for RWM control, an actuator located at the outer major radius of the plasma is favorable and should be effective.

According to ideal MHD, the RWM structure inside the plasma fluid is complex [Fig.13(a)]. However, when considering methods for stabilizing this mode, the fluid deformation is not the focus of attention. Instead, these methods focus on the magnetic field perturbation that is associated with the plasma fluid deformation, since a number of real time sensors are available to measure this perturbation (Fig.12) and relatively simple models of the RWM can be developed using this point of view. Various experimental studies [41]–[46] have revealed several characteristics of the RWM and their relation to ideal MHD predictions. Each of these will be discussed in more detail below.

1. The spatial structure of the RWM agrees with the ideal MHD theoretical prediction (Figs.14 and 15). The RWM exhibits a structure that is global, extending from the plasma core to outside of the vacuum vessel, where we consider the mode as represented by the combined magnetic fields of the plasma and conducting structures.
2. The existence of a threshold in plasma pressure for the onset of the RWM agrees with ideal MHD theory.
3. When a non-axisymmetric external field exists, the mode responds only to the component of the external field that matches the mode's own field structure. The mode amplitude is amplified proportional to the external field, behaving like a *magnetic field resonance* (to be discussed below).
4. Beyond the ideal MHD framework is a surprising observation: the mode can be completely stabilized by rotating the plasma, if the rotation is above a critical value.
5. The RWM can be stabilized by plasma rotation for well over the ideal MHD time scale (sidebar S19) and the mode spatial structure remains the same even after the wall eddy current disappears.

The sustainment of a single mode pattern over a long period is encouraging for developing simple magnetic control. This spatial invariance is often described as *mode rigidity*.

6. However, the finite amplitude of the long-sustained RWM reduces the bulk plasma rotation, leading to a less stable high-pressure plasma.

These observations provide the rationale for two different approaches to stabilizing the RWM. One approach is the use of feedback control to oppose the moving field that accompanies the growth of the mode. We will refer to this approach as magnetic control. The rate of growth of the mode is slowed sufficiently by the conducting wall to make a feedback process feasible. The existence of a single dominant mode allows for simpler models of the plant to be controlled. An example of the coil arrangement used to excite the non-axisymmetric field necessary for RWM control is shown with the DIII–D device in Fig.12.

Another approach for RWM control is the use of plasma rotational stabilization. In present day tokamaks, neutral beam injection (NBI, see sidebar S13) supplies an ample amount of angular momentum input for maintaining rotation of the plasma fluid, leading to the stabilization of the RWM mentioned above. However, it is not obvious whether sufficient plasma rotation can be achieved in fusion power generating reactors. Thus, magnetic feedback control is actively being pursued for use in future devices.

MODELS OF THE RWM INSTABILITY

In this section, we describe some of the basic models that are presently in use for development of methods for stabilizing the RWM. Initially, we assume that there is little or no bulk plasma fluid rotation and concentrate on only the magnetic aspects of the control problem. Models for magnetic control ignore the internal details of the plasma, focusing instead on the behavior of the magnetic field structure on the plasma surface. A common method of modeling the unstable mode is to replace the spatial perturbation of the plasma with an equivalent perturbation (in the sense that it produces the same magnetic field perturbation) of surface current on a spatially fixed plasma boundary. The surface current distribution is calculable from the geometrical shift of the plasma surface. The eddy current pattern on the wall can also be calculated once the plasma surface current pattern is determined. The plasma surface current and wall eddy currents are illustrated through plots of magnetic field normal to the plasma boundary in Fig.15.

Using the assumption of a rigid mode mentioned above, the spatial distribution of current on the plasma surface and on the wall remain intact while only their magnitudes change. Using the surface current representation of this mode, we can construct a state space model of the plant with states given by currents on the plasma surface, I_p, and in surrounding passive (wall) structures, I_w. These variables represent the scalar multipliers of the spatially fixed distributions of current on the plasma surface and in the wall. The external control coil current, I_c, represents the scalar multiplier of a single spatial distribution of currents produced by multiple coils chosen to best match the distribution

of the eigenmode. These variables all represent perturbations from axisymmetric (purely toroidal) equilibrium currents due to the appearance of the non-axisymmetric RWM in the plasma.

In the following, we discuss RWM behavior using a simple cylindrical model [47], [48]. Use of cylindrical models, in which plasmas are assumed to flow in an infinitely long cylinder, is a common first step in developing physics understanding of phenomena that occur in the "bent" cylinder constituting a torus.

The pressure balance on the plasma surface between the internal plasma pressure and the external magnetic field pressure leads to a circuit-like (sidebar S16) equation.

$$L_{eff}\, I_p + M_{pw} I_w + M_{pc} I_c = 0, \tag{1}$$

where constants M_{ab} represent mutual inductance between conductors a and b (Fig.16), the ef fective self inductance L_{eff} is given by

$$L_{eff} = \frac{L_p C_\beta}{(C_\beta + \Delta M)}\ , \qquad C_\beta = \frac{\beta_N - \beta_{N.\ no\text{-}wall}}{\beta_{N.ideal\text{-}wall} - \beta_{N.no\text{-}wall}}\ , \tag{2}$$

$\Delta M = L_p L_w / M^2_{pw} - 1$ is related to the wall stabilization effect, and L_p represents self-inductance of the plasma. The constant C_β is a measure of the stability of the plasma to resistive wall modes. When $C_\beta < 0$, β_N is below the no-wall limit and the RWM is stable. When $C_\beta > 1$, β_N is above the ideal-wall limit and the plasma cannot be (practically) stabilized. Efforts at active stabilization aim at the interval $0 < C_\beta < 1$. The wall eddy current and the active coil current are modeled by standard circuit (sidebar S16) equations

$$\begin{aligned} M_{wp}\dot{I}_p + L_w \dot{I}_w + M_{wc}\dot{I}_c + R_w I_w &= 0 \\ M_{cp}\dot{I}_p + M_{cw}\dot{I}_w + L_c \dot{I}_c + R_c I_c &= V_c\ . \end{aligned} \tag{3}$$

Here, constants R_α represent resistance in conductor *a* and, as in Eq.(1), constants $M_{\alpha b}$ represent mutual inductance and L_α represent self-inductance (Fig. 16). The ordinary differential and algebraic Eqs.(1) through (3) that constitute the overall circuit model can be expressed via a Laplace transform as

$$(Ms + R)\, I = V \tag{4}$$

where s is the Laplace transform variable and

$$M = \begin{bmatrix} L_{eff} & M_{pw} & M_{pc} \\ M_{wp} & L_w & M_{wc} \\ M_{cp} & M_{cw} & L_c \end{bmatrix}, \quad R = \begin{bmatrix} 0 & 0 & 0 \\ 0 & R_w & 0 \\ 0 & 0 & R_c \end{bmatrix}, \quad I = \begin{bmatrix} I_p \\ I_w \\ I_c \end{bmatrix}, \quad V = \begin{bmatrix} 0 \\ 0 \\ V_c \end{bmatrix}.$$

Using this formulation, we can treat the RWM control model as if it were a standard circuit equation. The mutual inductances are computed by standard geometric methods [49]. The modified self-inductance L_{eff} is the only term that differs from the standard electromagnetic definition (see sidebar S16, for example) and includes the plasma parameters. This approach allows variations in the plasma to be modeled as changes to a single term L_{eff} in the model.

ROTATIONAL STABILIZATION

It has been observed on DIII–D that when the toroidal rotation of the bulk plasma fluid remains above 6kHz (thousands of rotations per second) the RWM instability is completely stabilized (Fig.17). One of the primary causes of rotation in current experimental devices is the injection of neutral deuterium atoms (intended originally for heating; see sidebar S13) at an angle nearly tangential to the torus. The momentum of these particles is imparted to the bulk plasma, thereby increasing the rotation. Distinct from the fluid rotation is the rotation of the mode itself, typically at a frequency between 10 and 20Hz, that is believed to be coupled to the fluid rotation.

To include the effect of plasma rotation in the model of the RWM, we must depart from the previous assumption of a *rigid mode at a fixed toroidal angle*, with the special case of zero rotation represented by the previous discussion. The unstable mode still maintains the rigid sinusoidal current spatial distribution having toroidal period one (Fig.15), but now may be shifted or rotating in toroidal angle. Thus the previous representations in which $I_c(t)$, $I_p(t)$, and $I_w(t)$ were scalar multipliers of spatially fixed current distributions are replaced by two parameter multipliers of the form $I^*(t) = A^*(t)e^{i\phi^*}(t)$, where $\phi_*(t)$ represents the toroidal angle of the sinusoidal distribution with respect to a fixed reference angle. Now the currents I_c, I_p, and I_w as well as perturbed magnetic fields due to the wall B_w and due to the plasma surface B_p are each represented by complex numbers whose real and imaginary parts represent sinusoidal distributions with peak amplitude in the 0 and 90deg toroidal directions, respectively. In this notation, multiplication by $i = \sqrt{-1}$ represents a result that is rotated toroidally by 90deg.

In general, the mechanisms for combined rotation and magnetic effects on the RWM are not well understood. Using an argument that seeks to account for the exchange of energy between the plasma mode and external conductors, Chu, et al. [50] propose the model

$$(\delta W_{Iw} + i\Omega_\phi D)\, B_p = C_{pw}\, B_w \quad , \tag{5}$$

to represent the coupling between changes in field B_p at the plasma surface and changes in field at the vessel wall when the plasma is rotating. This model is only qualitative and still somewhat speculative, but is described here to provide some insight into the possible mechanisms for experimentally observed rotational stabilization. Here, Ω_ϕ represents the plasma fluid toroidal rotation frequency and $C_{pw} = M_{pw}^{-1}$ is the inverse of the mutual inductance between the wall and the plasma surface. The quantity δW_{Iw} represents the coupling of RWM energy transferred through the field B_p produced by the plasma to the component of the field B_w that is toroidally in phase with B_p, while $\Omega_\phi D$ represents the energy coupled to the component of B_w that is 90deg toroidally advanced. The quantity D represents an unknown dissipation mechanism. This representation is motivated by the following:

1. Experiments show that, when the plasma is rotating, the RWM responds at a different toroidal angle than the angle at which an external field is driven. For example, when the plasma is at steady state with a stable RWM ($\beta_N < \beta_{N,\,no\text{-}wall}$), if a fixed sinusoidal n = 1 current $I_c(t) = A_c e^{i\phi c}$ is applied (so that eddy currents are not excited in the wall), the plasma surface mode responds not at the angle $\phi_p = \phi_c$ but at an angle $\phi_p = \phi_c + \delta\phi$ with $\delta\phi > 0$ [44].
2. A theoretical consideration is that momentum can be exchanged between the toroidally rotating plasma and the RWM, resulting in a transfer of some of the unstable mode's energy to a different toroidal angle (see the discussion that follows).

There are several candidate models for the dissipation mechanism D, but none has been satisfactorily verified yet experimentally. We present here a rather simplistic explanation of one candidate model that is consistent with the three experimentally observed phenomena: (1) the increase in RWM growth rate as the plasma fluid rotation slows to a critical rotation value, (2)the observed much slower rotation of the RWM itself in the same direction as the rotation of the bulk plasma fluid, and (3) the response described above of a stable RWM to an applied n = 1 perturbation that appears at a toroidally shifted location. A more accurate and complete model requires significant background preparation, so will not be presented. The proposed model postulates a coupling between the unstable mode and bulk plasma fluid through a form of viscous friction, as follows. Current is defined as the rate of flow of charged particles. In a current-carrying plasma, an RWM fluid deformation (Fig.11) may be thought of as a change in the pattern of flow of the charged particles that comprise the current in the plasma. This change in flow is seen outside the plasma as a change of flux or field at magnetic sensors. This flow of particles is driven by the sharp difference in total (plasma plus magnetic) pressures inside and outside of the plasma — the driving force of the RWM instability — and a significant portion of this flow is radially directed (Fig.18). The motion of particles in the plasma can also be influenced by the injection of momentum (from neutral beams for example). The toroidal particle flow introduced by toroidal momentum injection interacts with the particle flows caused by the RWM and vice versa through collision interactions. To sustain the RWM in a given direction, work is required by the RWM instability to move particles against this toroidal

particle flow. This resistance to the motion of particles is essentially the mechanism of viscous friction. The RWM's loss of energy through this work is the proposed damping mechanism. Assuming this damping mechanism, the model Eq.(5) can be included in the Eq.(4) by modifying L_{eff} [45]

$$L_{eff} = \frac{L_p\,[C_\beta + \alpha_\phi\,(s + i\,\Omega_\phi)]}{[C_\beta + \alpha_\phi\,(s + i\,\Omega_\phi) + \Delta M]} \quad , \tag{6}$$

where α_ϕ represents the viscous drag coefficient.

THE ROLE OF ERROR FIELDS

Rotation of the bulk plasma is influenced significantly by the level of error field present in the device. The error field is defined as the difference between the slightly non-axisymmetric magnetic field produced by an as-constructed device and the ideal axisymmetric field that would be produced by an ideally constructed device. The component of the error field resonant with the RWM is that portion of the error field that matches the field pattern of the unstable eigenmode on the plasma surface.

This resonant error field can be represented as an external current source I_e acting in a manner similar to the external control coil current I_c. The impact of this field can thus be described by replacing I_c by I_e in the plasma response Eq.(1). Since the error field is steady state, the perturbed quantity $I_w = 0$ if the RWM is stable. (A *changing* current, either I_p or I_e, is required to induce nonzero eddy currents I_w.) In this case, the plasma response, I_p, to the error field is also steady state, given by Eq.(1) as

$$I_p = -(M_{pe}/L_{eff})I_e \quad . \tag{7}$$

Since M_{pe} is real, the toroidal phase shift, $\delta\phi$, is given by Eq.(7) as $\delta\phi = \tan^{-1}[-\mathrm{Im}(L_{eff})/\mathrm{Re}(L_{eff})]$. It is clear that the magnitude of the plasma response can reach a huge value around the no wall limit where $L_{eff} \approx 0$, similar to a resonance effect. This phenomenon is known as *Resonant (Error) Field Amplification* (RFA). As the growth rate of a stable RWM approaches zero from below, the value of L_{eff} also approaches zero. Thus RFA increases as a stable RWM becomes less stable.

The non-axisymmetric error field and the resulting amplification of the stable RWM are believed responsible for the rotation slowing observed in Fig.17 through a form of *magnetic braking* of the plasma rotation. As with rotational damping, there is more than one possible mechanism for the observed rotational slowing. One rather well accepted explanation uses an analogy with the induction motor. An induction motor consists of a conductive rotor (the inside part that turns) surrounded by a stator (the stationary outside part that causes it to turn). A magnetic field that rotates around the rotor is set up by properly phased currents flowing in a set of coil windings in the stator. As long as this moving magnetic field rotates faster than the rotor, the field acts on the conductive rotor to

generate currents on its surface. A torque is produced on the rotor through the interaction of this induced current with the rotating field (the "I cross B" force; see sidebar S17). If the magnetic field produced by the stator becomes stationary or reverses direction while the rotor is rotating, the applied torque reverses direction and causes the rotor to slow down. This is directly analogous to a rotating (conductive) plasma interacting with a stationary non-axisymmetric magnetic field such as an error field. Slowing of the plasma by the error field and RFA causes a stable RWM to become less stable, which then increases the effect of the magnetic braking, which slows the plasma even more. This process continues until, eventually, the RWM becomes unstable as shown in Fig.17.

To the sophisticated reader, it is clear that both the rotational damping and the induction motor analogy describe forces that are exerted in both directions. For example, the viscous damping mechanism discussed in the previous section that stabilizes the RWM also results in forces that tend to slow the plasma rotation. Several damping/slowing mechanisms have been proposed, but present experimental data is not sufficient to clearly confirm or refute these proposals. It is also possible that more than one of these mechanisms will ultimately be determined to play a major role.

MAGNETIC CONTROL APPROACHES

Experimental approaches for magnetic control presently include correction for external error fields to reduce the magnetic braking on rotation and, separately, magnetic feedback stabilization of the RWM in the absence of plasma rotation. The magnetic feedback efforts allow for mode rotation but generally do not account for fluid rotation effects. The situation of magnetic feedback with non-zero plasma fluid rotation is not yet well enough understood to develop useful control approaches. An experimental RWM controller consists of the observation sensors, sensor logic, digital controller, power supplies, and actuator coils.

Actuators consist of actively driven current-carrying coils, typically with a picture frame geometry (Fig.12). The rigidity of the mode simplifies the discussion of the required feedback field. When non-axisymmetric field is applied, the plasma perturbation responds only to the component of the field that matches its own mode structure. This implies that the external coils (C-coils), which primarily produce radial field, are not very efficient since at least half of the magnetic energy does not couple with and therefore does not affect the helically shaped mode. The connection flexibility of the internal coil (I-coil) set can be used to provide a field pattern (Fig.15) that more closely matches that of the RWM. The I-coils have the additional advantages that they are closer to the plasma while the appearance of C-coil flux at the plasma is delayed due to shielding by eddy currents in the vessel. For these reasons, the internal coil set is superior to the external coils for feedback control.

Although error fields are determined by the limited accuracy of device construction and are independent of the plasma, the required compensation for these fields depends on properties of the plasma being maintained because of the RFA. The necessary spatial distribution of applied corrective field is related to the MHD mode structure and the required magnitude of the correction depends on

the value of L_{eff} according to Eq.(7). The magnitude and the mode toroidal angle can evolve slowly in time during the discharge because of changes in plasma properties. In addition, the error field has a complicated non-axisymmetric distribution that cannot be completely canceled by a finite number of actuator coils. Thus, compensation cannot be done open loop based on a priori calculations. This motivates the use of *dynamic error field correction,* which adjusts the error field correction based on the plasma mode response. This leads to a slow time-scale (much slower than the wall time) feedback process. Magnetic control aimed at directly stabilizing the RWM requires feedback with a faster time constant equal to a fraction of the wall time. Thus requirements on actuating coils and power supplies are very different for error field correction and for magnetic feedback stabilization.

Power systems for tokamak control problems are a challenge due to simultaneous requirements for high voltages and currents and speed of response. RWM control requires a relatively high current (a few kiloamps) at near steady state to compensate for error fields and, simultaneously, a fast (a few hundred hertz) lower current response to provide magnetic feedback stabilization. Since the conductive wall slows the mode growth to approximately the time constant of the wall, the maximum bandwidth required for the supply is defined by the inverse of this wall time constant. For example, the DIII–D power supply is designed to have a 3dB bandwidth of 500Hz in order to stabilize plasmas with values of β up to halfway between the no wall and the ideal wall limits ($C_\beta = 0.5$).

There have been several methods investigated for detecting the mode growth and determining the toroidal angle. All are based on the experimental observation that the RWM is well defined by an n = 1 distribution and the mode structure is reasonably rigid so the mode can be represented by an amplitude perturbation that varies sinusoidally in the toroidal direction. The mode can thus be represented by two parameters: the mode amplitude and toroidal angle, or sine and cosine components $A^{cos}(t) = A(t)\cos[\phi_0(t)]$ and $A^{sin}(t) = A(t)\sin[\phi_0(t)]$ where ϕ_0 is the time varying unknown toroidal angle of the mode amplitude maximum. Methods investigated to identify the two parameters consist of matrix multiplications $[A^{cos}(t) \;\; A^{sin}(t)]T = Gx$ where x is a vector of sensor measurements and is a constant gain matrix. One approach is to use radial flux sensor measurements $x(t) = [\psi_1(t) \; \psi_2(t) \;\; \psi_3(t)]^T$ at the same radius and at different toroidal angles. Each $\psi_j(t)$ represents the difference in magnetic flux measured at two sensors located at same radius but 180deg apart toroidally at the midplane of the torus. This differencing is done to reinforce radial flux measurements due to an n = 1 mode perturbation while de-emphasizing flux contributions from disturbance sources (such as plasma perturbations having toroidal mode structure with n even). This scheme is called *smart shell* because the feedback process attempts to minimize the total flux perturbation at the observation point so as to emulate a perfectly conducting wall at that radius.

Another approach is to use only poloidal field sensors $x(t) = [B_1(t) \;\; B_2(t) \;\; L \;\; B_m(t)]^T$ where each $B_j(t)$ represents the difference in magnetic field measured at two sensors located at same radius but 180deg apart toroidally at the midplane of the torus (Fig.12). This difference is also used to reinforce poloidal field measurements due to an n = 1 mode perturbation and to remove field contributed by axisymmetric variations in the plasma (such as in the plasma shape). This approach

is called *mode control* because the poloidal field sensor measures almost no field directly from the actuator coils, which produce primarily radial field, and thus is more sensitive to the field variations due only to the plasma mode.

A third approach is to determine the mode amplitude and phase using all available flux and poloidal field sensors $x(t) = [\psi_1(t) \quad \psi_2(t) \quad L \quad \psi_{n_\psi}(t) \quad B_1(t) \quad B_2(t) \quad L \quad B_{n_B}(t)]^T$ rather than just symmetrically located pairs of either type. Here, the fluxes $\psi_j(t)$ and fields $B_j(t)$ are measurements at individual sensor locations. This is referred to as the *matched filter approach* [51] because each row of G defines a spatial matched filter. The first row is matched to the normalized response expected in the set of sensors from a mode with phase $\phi_0 = 0$ while the second row is matched to the normalized expected response from a mode with phase $\phi_0 = 90$deg. Use of a matched filter was motivated by experimentally observed difficulties in rejecting noise and disturbance signals. Rejection of measurement noise could be enhanced by averaging multiple sensors obtained with the matched filter. The most severe disturbance was due to magnetic sensor responses to edge localized modes (ELMs — see the next section of this article). An ELM is a local mode whose spatial magnetic field distribution is significantly different than the distribution defined by the global RWM, making it a good candidate for rejection via a matched filter. Use of the matched filter in simulations has been shown to improve the accuracy of the mode estimation, but it does not provide a complete solution to rejection of ELM disturbances. The primary difficulty is that, on short time scales, the growth of an ELM disturbance signal includes a large n = 1 component similar to the unstable n = 1 RWM. The ELM excitation mechanism and mode structure are significantly different however. This motivated work on development of a Kalman filter to exploit information contained in the RWM dynamics model to filter out the ELM signals. Simulations [52] indicate that combining the spatial matched filter and dynamic Kalman filter will significantly improve signal-to-noise ratio and reject ELM disturbances. Use of the matched filter and the Kalman filter require relatively detailed knowledge of the mode spatial distribution. Use of a Kalman filter requires, in addition, a good model of the time evolution dynamics of the mode and its interaction with surrounding structure. The mode dynamics depend strongly on the fluid rotation frequency, however, and this dependence has not been well characterized. Thus the experimental application of this approach relies on the success of ongoing efforts to develop models that combine MHD and rotation effects.

Experimental controllers have been limited so far to the use of proportional, integral, and derivative (PID) algorithms. PID and more advanced control algorithms have also been studied in simulations and paper studies [53]. Experimental use of the more sophisticated control algorithms has not been pursued because of the ambiguity in models due to incomplete understanding of dependence of the RWM on rotation.

EXPERIMENTAL PROGRESS IN STABILIZING THE RWM

The most important progress in RWM stabilization was the sustainment by rotation of a discharge

with $C_\beta \approx 1$ using open loop preprogrammed non-axisymmetric coil currents to minimize error fields. The program for this current was determined from the heavily time-averaged coil current signal previously obtained in a nearly identical plasma discharge that used dynamic error field correction to define the coil currents. With feedback off and non-axisymmetric currents programmed in this way, the discharge behavior followed closely the evolution of the discharge with feedback on; the achieved values of β_N and plasma rotation frequency were nearly identical. This evidence suggested that the resonant component of the non-axisymmetric field contributed significantly to the mode amplification and, consequently, reduced the rotation velocity. Once the compensation was made through the dynamic error field correction, the RFA amplitude did not grow and the plasma did not slow down. The resulting plasma rotation was sufficient to suppress the onset of RWM up to the ideal wall β_N limit.

Several experiments [43] have shown an extension of discharge duration when using magnetic feedback, but have not demonstrated long term stabilization. Analysis [54] and experiments [55] are consistent in showing the superiority of mode control over smart shell control. Motivated by analyses of coil/sensor effectiveness ([56],[57]), the DIII–D device has been equipped with actuators located both inside and outside the vacuum vessel. Use of the internal coils (I-coils) has significantly improved magnetic feedback performance over that achievable with external coils (C-coils) alone (Fig.12).

FUTURE DIRECTIONS

Experimental and theoretical research continues on this important control problem. Many important issues are near to being resolved, including the most effective type, location, and configuration of actuators and sensors for magnetic feedback control. Although not yet sufficient for a complete model, a great deal has also been learned about the dynamics of the RWM and its interaction with error fields and plasma fluid rotation. Efforts have also begun to address some of the more practical issues such as required current levels, power supply response times, and communication delays that are required for magnetic feedback systems.

Significant effort remains to complete RWM model development. Sufficient experimental data needed to either confirm or refute the many candidate magnetic feedback models has been difficult to obtain because of the interaction between error fields, fluid rotation, mode growth, and magnetic feedback. Once models are completely developed and validated, the final algorithm(s) for control that can handle the wide range of RWM conditions will need to be developed and experimentally tested. This will be challenging, since the RWM growth time can vary from a fraction of wall time (a fraction of millisecond) to the angular momentum confinement time (a fraction of second). In addition, the present linear rigid mode growth assumption represents only the dominant mode of several potentially unstable modes; even this dominant mode may become nonlinear nearer to the ideal wall limit. Another important near term objective is the need for extrapolation of RWM stabilization methods to ITER and reactor oriented devices.

CONTROL OF PLASMA PROFILES AND INTERNAL TRANSPORT BARRIERS

The requirements of ITER and the need to optimize the tokamak concept for the design of an economical — possibly steady state — fusion power plant have motivated extensive international research on plasma transport (see Fig.9 caption) and confinement in toroida l devices. These investigations have aimed at finding plasma regimes with improved confinement with respect to the one predicted by typical tokamak scaling laws and have led to the definition of the Advanced Tokamak (AT) operation scenarios (sidebar S18) [58]. In a large number of machines, experiments have demonstrated the existence of such regimes that allow access to a high confinement state with improved MHD stability and leading to a strong increase of the performance as quantified by the energy confinement time and plasma pressure (τ_E and β_N; see sidebar S2). In such conditions a dominant fraction of the plasma current is self-generated by the bootstrap mechanism (sidebar S15), which reduces the requirement for externally driven non-inductive current for steady state operation. This bootstrap current is favored by the generation in the plasma of an internal transport barrier (ITB) [59], a region where particle and heat transport are strongly reduced. An ITB is characterized by large pressure gradients and by the presence of a visible
"break" in the slope of the electron and/or ion temperature profiles similar to the edge transport barriers (ETB; sidebar S12). ITBs are often combined with an ETB, which gives rise to a pressure pedestal at the plasma edge, characteristic of the H–mode [60] (sidebar S11).

Although the formation mechanism of ITBs has not been entirely identified, significant progress has been made in understanding them. Many recent studies have shown the key influence of the safety factor profile q(x) (x = r/a; see sidebars S4 and S5) for the triggering of barriers. Both the radial profile of the magnetic shear (sidebar S20) and the location of the flux surfaces where q is rational have been shown to be essential for the emergence of ITBs [61]–[63].

When ITBs become too strong, the steep pressure gradient characteristic of the ITB may exceed some MHD stability limit, leading to the loss of the confinement or even to plasma disruption (sidebar S14). Thus, the promising concept of a steady-state tokamak reactor may only be realizable if stationary ITBs can be sustained in a stable way. This has motivated a large experimental effort at JET, aiming at the real-time simultaneous control of the safety factor, temperature, and pressure profiles. This section reviews the progress achieved, based on material published in Refs. 64–68.

S15. BOOTSTRAP CURRENT (SIDEBAR)

The bootstrap current is an equilibrium current that is self-generated (without the need of an imposed electric field) in a toroidal plasma. In a tokamak plasma, the guiding center [the center of the fast Larmor gyro-motion (see Fig.9 in the intro article)] of most particles follow approximately helical orbits that encircle both the major axis of the torus (vertical axis) and the magnetic axis of the plasma (see Fig.14 in the intro article). This periodic guiding center motion is the combination of free streaming along the helical magnetic field lines (Fig.10 of the intro article) and of small radial drifts due to the gradient and curvature of the magnetic field, which average to zero after a complete

period. However, the toroidal magnetic field intensity produced by external coils in a tokamak decreases as 1/R (R being the distance to the major axis) and therefore particles encounter varying field intensities along their orbits, from a minimum, B_{min}, on the outer radial part of the helical orbit (called the *low-field* side of the torus) to a maximum, B_{max}, on the inner radial part (called the *high-field* side of the torus). As a result, particles with low velocity parallel to the helical field lines (whose kinetic energy, W, is mainly in the Larmor motion, $W \approx W_{\perp}$, orthogonal to the field lines) cannot complete a helical trajectory around the magnetic axis as this would violate the conservation of both their energy W and magnetic moment ($\mu = W_{\perp}/B$) along the orbit. At some point their parallel velocity must vanish and change sign and therefore these particles are trapped on the low field side of the torus where their guiding centers describe banana-shape orbits (see Fig.19). Particles that are able to complete their helical orbit are called *passing particles*, as opposed to the *trapped particles*. In the presence of a density gradient and at a particular location in the plasma, there are more trapped particles going in one toroidal direction [trajectory (a) in Fig.19] than in the other one [trajectory (b)] and therefore the local ion and electron velocity distributions are anisotropic. Therefore, each trapped particle assembly (trapped particles of a given species passing through point P) carries a finite toroidal momentum proportional to the density gradient at P. Now, particle collisions give rise to a continuous exchange of momentum between trapped and passing particles. For instance, passing electrons, which make up the bulk of the electron population, receive net toroidal momentum from the anisotropic trapped electrons at an effective rate that is much faster than the rate at which they lose momentum to the bulk ions. Therefore a net equilibrium electron current results. An additional contribution, with the same sign, comes from the passing ions. This net positive current is known as the bootstrap current.

A technique that is currently used to produce ITBs on JET [69] is the application of lower hybrid heating and current drive (LHCD) (sidebar S13) during the low density plasma current ramp up phase (see Fig.8 in the intro article), prior to the high performance phase of a discharge in which high power heating is applied. By this method, often referred to as LHCD preheating, certain populations of resonant electrons are unidirectionally accelerated by electromagnetic waves so that the current density profile (sidebar S20) is made broader and sometimes even hollow (lower at the center than near the edge), depending on the applied power. In such a case, the q-profile becomes non-monotonic in the core of the plasma at the time of application of the main heating power and the magnetic shear (sidebar S20) is said to be reversed as it changes sign. Two different methods are used for the main plasma heating in JET, ion cyclotron resonance heating (ICRH) and neutral beam injection (NBI) (sidebar S13). At present, the total injected power can reach up to 25MW. An interesting advantage of the additional LHCD when it is also applied during the main heating phase is its ability to maintain the preformed broad current profile almost stationary during the main heating phase, whereas it would otherwise peak in the plasma center with a characteristic time scale given by the resistive diffusion time (relaxation time of the profile needed to reach a steady state; sidebar S19). This peaking tendency is due to the fact that plasma temperature is higher in the

core and plasma resistivity (sidebar S13) is inversely related to temperature. The effect of the LHCD is to slow down, and possibly stop, the temporal evolution of the current profile peaking [70]. This also allows avoidance of some instabilities or disruptive events related to the presence in the plasma of magnetic flux surfaces where q is a rational number (such as NTMs for example).

To control, it is necessary to characterize the ITB in a quantitative way. For that purpose a local criterion characterizing the location, strength and dynamics of ITBs in JET has been developed, which can be computed in real time from the ion and electron temperature measurements. This will be described in the following section with the first experiments of ITB strength control that were performed in JET.

INITIAL EXPERIMENTS ON ITB CONTROL IN JET

The objective of the initial ITB control experiments was to investigate practical methods of sustaining ITBs in a controlled and reproducible way in order to take full advantage of the resulting confinement improvement. The goal was to tune the applied heating power so as to maintain the transport barrier and the plasma in a stable state during long periods of time, although not necessarily in steady state. One difficulty in achieving such a goal was to find an objective way to satisfactorily quantify the ITB behavior. For that purpose, a local criterion characterizing the presence, location and strength of ITBs has been developed. The criterion is quantified by calculating the ratio, ρ^*_T, of an ion Larmor radius, ρ_i(Fig.9 of the intro article), to the temperature gradient scale length, $(\nabla T/T)^{-1}$. Using an analysis of an experimental JET database, it has been shown [64] that an ITB is most likely to exist at normalized radius, x = r/a (sidebar S5), and at time t, when

$$\rho^*_T(x, t) = -\rho_i\,[\nabla T(x, t)/T(x, t)] > \rho^*_{ITB} \quad , \tag{8}$$

with the threshold value $\rho^*_{ITB} \approx 0.014$. (Here, $\nabla T = \delta T/\delta x$; see sidebar S5.) The proposed criterion enables detection of the presence of an ITB at a given normalized radius with a large degree of confidence when $\rho^*_T(x, t)$ exceeds the fixed threshold value. In JET, transport barriers are generally observed simultaneously on both the ion and electron heat transport channels, i.e., on the ion temperature gradient (ρ^*_{Ti}) as well as on the electron temperature gradient (ρ^*_{Te}). For specificity, we shall refer to the latter — identified through Eq.(8) applied to ρ^*_{Te} — as an electron transport barrier or electron ITB, so that

$$\rho^*_{Te}(x, t) = -\rho_i\,(\nabla T_e/T_e) > \rho^*_{ITB} \quad .$$

Electron transport barriers have been controlled in real-time using the maximum value of the parameter $\rho^*_{Te}(x, t)$ across the plasma radius (x) as the controlled output variable and one power actuator only. Best results were obtained when using the ICRH system as the actuator. The temperature measurements from which ρ^*_{Te} was calculated were made with an heterodyne radiometer

using the electron cyclotron emission (ECE) from the plasma [71]. A simple proportional-plus-integral (PI) feedback was used to compute the required actuator input power

$$P(t)[MW] = P(t_0) + G_p\, DX(t) + G_I \int_{t0}^{t} \Delta X\,(u)\, du$$

where $X(t) = \max[\rho^*_{Te}(x, t)]$, $P(t_0)$ is the actuator power at the initial time t_0 of the control, ΔX is the difference between the target output value (setpoint) and the measured output signal X(t), and G_p and G_I are the proportional and integral gains, respectively. The strategy for control of the ITB through control of X using only one actuator (the ICRH heating system) assumes that during the control phase, the current profile (equivalently, q-profile), which has been identified as an essential parameter for the ITB dynamics, does not evolve significantly. This simple strategy is therefore valid only for periods of time that are shorter than the resistive current diffusion time (around 20 seconds or more in JET; sidebar S19). The high power control phases in control experiments were always limited to 10s.

In a second set of experiments, the additional effect of a second independent feedback loop to control plasma pressure at the magnetic axis was studied with the aim of combining the ITB confinement improvement with high-β (sidebar S2) plasma stability and thus avoiding plasma disruptions. This additional control was achieved by measuring the Deuterium-Deuterium (D-D) fusion reaction rate and using neutral beam injection (NBI) as the actuator. (The neutron production from the D-D reactions is strongly correlated with the central plasma pressure.) An experiment with simultaneous control of ρ^*_{Te} — with ICRH — and of the D-D reaction rate — with NBI — is depicted in Fig.20 [65]. This control was obtained with a constant LHCD power (3MW) throughout the pulse, which also demonstrated the important role played by LHCD in slowing down the current density profile evolution (Fig.21) and improving the long-pulse stationarity of these advanced discharges. It was found that setting-up a suitable q-profile, characterized by a weak or even reversed magnetic shear (sidebar S20), seems to be a key condition for triggering an internal transport barrier that can then be controlled with the concomitant improved plasma confinement. In order to improve the control of the ITB and to allow extended control duration and, later, extrapolation to steady state burning plasma devices such as ITER, control of the q-profile was therefore needed.

CONTROL OF THE CURRENT DENSITY PROFILE

The experimental investigations described in this section were the first attempts in JET at controlling the q-profile. (Controlling the q-profile and the current profile are basically equivalent — see sidebar S20.) To start, the controlled safety factor profile was simply characterized by its values at five discrete fixed radii, these values being considered as an adequate set of lumped parameters to fully describe the system. They were calculated in real time using magnetic measurements together with data from an interferometer-polarimeter diagnostic, which allowed a fairly accurate reconstruction of the magnetic equilibrium in real-time [66]. The three heating and current drive powers, P_{LHCD},

P_{ICRH} and P_{NBI} were used as actuators for the control. A linearized model was obtained experimentally by performing dedicated open-loop experiments and varying the input powers. A linearized Laplace transform model of the form

$$\delta Q(s) = K(s)\, \delta P(s) \quad , \tag{9}$$

was assumed around a reference plasma steady state, where δQ is a (5×1) vector that represents the change in the safety factor from the reference state when the (3×1) input power vector changes by δQ. The problem was thus reduced to identifying the (5×3) matrix and finding a suitable pseudo-inverse. The steady-state gain matrix was determined to be sufficient and was deduced experimentally from simple power steps (from the reference state) in dedicated open loop discharges. In order to design a PI feedback controller that maximizes the steady state decoupling of the multiple feedback loops and ensure minimum (in the least square sense) steady-state offset, a truncated singular value decomposition (TSVD) of the steady state gain matrix, , retaining only two principal components of (the third one being associated with a very small singular value) was used [67]

$$K(0) \approx W \bullet V^T \quad ,$$

(with V^T the transpose matrix of V). This provides steady state decoupling between modal inputs $\alpha(s) = V^T\, \delta P(s)$, and modal outputs $\beta(s) = W^T\, \delta Q(s)$. Pseudo-modal control techniques could then be used by inverting the diagonal steady state gain matrix, Σ. Thus, the PI controller transfer function matrix was chosen as follows:

$$\begin{aligned} \delta P(s) &= g_c[1+1/(\tau_i s)]\, G(s)\, [\delta Q_{target} - \delta Q(s)] \\ &= g_c[1+1/\tau_i s)]\, V \bullet^{-1} W^T [\delta Q_{target} - \delta Q(s) \quad , \end{aligned}$$

where g_c is the proportional gain and (g_c/τ_i) is the integral gain. These experiments were the first to use three heating and current drive systems to control the q-profile in an ITB tokamak scenario with a significant fraction of the plasma current carried by the bootstrap current. Because of the long current diffusion time scale, the plasma pulse had to be as long as possible for the effectiveness of the controller to be fully assessed (sidebar S19). Therefore a plasma scenario (sidebar S18) that had been developed for long pulse studies was selected. Figure22 shows the result of a closed-loop experiment in which the target q-profile had a slightly reversed magnetic shear (sidebar S20) in the plasma core. The control was applied between t = 7s and t = 13s, with initial powers at the start of the control phase of 2.5MW for LHCD, 7MW for NBI and 3MW for ICRH. These powers were chosen sufficiently below the power limits of the systems to avoid possibly hitting the saturation of an actuator during the closed-loop experiments. The powers requested by the controller and delivered by the three systems are shown in Fig.23.

The demonstration of real-time control of the q-profile encouraged new efforts to develop an integrated ITB control, which would include both the current and temperature gradient profiles

(sidebar S20). These two non-linearly coupled profiles are believed to be essential ingredients governing ITB physics. The most recent profile control experiments performed in JET therefore used an extension of the previous model-based technique to control simultaneously q(x) and $\rho^*_{Te}(x)$considered as distributed parameters characterizing the current and temperature gradient profiles, respectively.

In this case, a discretized representation of their response to the three power inputs (NBI, ICRH, LHCD)
can be written in matrix form

$$\delta G(s) = K(s)\delta P(s) \quad ,$$

similar to Eq.(9) and a controller can be derived as described above. (See sidebar for details.) Here, $\delta G(s)=[G_{\delta_{q1}}(s) \ \mathrm{L} \ G\delta q_{n_a}(s) \ G\delta\rho^*_{T_{e1}}(s) \ \mathrm{L} \ G\delta\rho^*_{T_{enb}}(s)]^T$ represents a finite set of coefficients of two sets of basis functions $a_i(x)$, i=1, 2, ..., n_α and $b_i(x)$, i=1, 2, ..., n_α that approximately span the set of achievable q and ρ^*_{Te} profiles, respectively [68] (Fig.24). The PI controller structure was defined as

$$\delta P(s) = g_c[1+1/(\tau_i s)]K_{inv}\,[\delta G_{target}(s) - \delta G(s)] \quad , \qquad (10)$$

where g_c is the proportional gain, (g_c/τ_i) is the integral gain, and K_{inv} is a particular pseudo-inverse of the steady state gain K(0) (see sidebar).

TECHNIQUE FOR DISTRIBUTED-PARAMETER CONTROL (SIDEBAR)

In summing up the complexity of plasma transport phenomena around a reference plasma state into a simple linearized model having only three degrees of freedom (corresponding to three actuators), one should take into account as much information on the spatial structure of the physical system to be controlled as possible. This can be achieved by retaining the distributed nature of the problem both in the model identification and in the control algorithm.

Also, to design a controller for an ITB regime, the plasma response must be linearized around a stationary reference state presenting an ITB. The current density and temperature gradient profiles were controlled via the safety factor profile, q(x, t), and the parameter ρ^*Te(x, t), respectively. The variations $\delta q(x, s)$ and $\delta\rho^*_{Te}(x, s)$ (s is the Laplace-transform variable) around the reference stationary state can be represented as a (2×1) profile vector $\delta Y(x, s)$

$$\delta Y(x, s) = \begin{bmatrix} \delta q(x, s) \\ \\ \delta\rho^* T_e(x, s) \end{bmatrix} .$$

Assuming a time-independent process, the linearized response of the two-function-vector $\delta Y(x, s)$ to the variation of the heating and current drive powers

$$\delta P(x, s) = \begin{bmatrix} \delta P_{LHCD}(x, s) \\ \delta P_{NBI}(x, s) \\ \delta P_{ICRH}(x, s) \end{bmatrix} .$$

can be written, without loss of generality, in the integral form

$$\delta Y(x, s) = \int_0^1 K(x, x', s)\, \delta P(x', s)\, dx'$$

where the kernel K(x, x', s) is to be determined. This kernel is assumed to be square-integrable so that it admits an infinite singular value decomposition:

$$K(x, x', s) = \sum_{i=1}^{\infty} \sigma_i(s)\, W_i(x, s)\, V_i^T(x', s) \quad ,$$

where V_i^T (x, s) are the transposes of an infinite set of (3×1) matrices of functions, V_i(x, s), in the input space, W_i (x, s) are (2×1) matrices of functions in the output space, and σ_i(s)are the corresponding positive singular values.

The essence of the method is to identify the best experimental approximation of this kernel by means of its dominant singular elements, or principal components, and to use this approximation to define a suitable controller. The δq(x, s) and $\delta\rho^* T_e$(x, s) profiles are thus approximated by their projections on finite dimensional spaces using the so-called Galerkin scheme

$$\delta q(x, s) = \sum_{i=1}^{n_a} Gq_i(s)\, a_i(x) + R\delta q\,(x, s) \qquad \textit{and}$$

$$\delta\rho^* T_e(x, s) = \sum_{i=1}^{n_b} G\rho^* T_e(s)\, b_i(x) + R\delta\rho^* T_e(x, s) \quad ,$$

where n_a and n_b the dimensions of two subspaces spanned by two sets of basis functions, a_i(x) and b_i(x), Gq_i(s) and $G\rho^*_{T_{ei}}$(s) are the so-called *Galerkin coefficients* of those basis functions, and Rδq(x, s) and $R\delta\rho^*_{Te}$(x, s) are the two residuals that are orthogonal to the basis functions α_i(x) and b_i(x), respectively.

In the same way δP(x, s) can be written as follows:

$$\delta P(x, s) = C(x)\, \delta P(s) \quad ,$$

with δP(s) containing the three power variations from the reference steady state powers

$$\delta P(s) = [\delta P_{LHCD}(s) \quad \delta P_{NBI}(S) \quad \delta P_{ICRH}(s)] \quad ,$$

and C(x) is a diagonal matrix containing three normalized power deposition profiles.

Anticipating that only three singular values can be found with only three independent actuators,

the SVD of the kernel K (x, x', s) can be truncated as follows

$$K_t(x, x', s) = \sum_{i=1}^{3} \sigma_i(s) W_i(x, s)\, V_i^T(x', s) \quad ,$$

where only the singular vectors associated with the three largest singular values are retained. Projecting the singular vectors on the corresponding basis functions, a matrix relation between the new outputs (Galerkin coefficients) and the inputs (power modulations) can be obtained

$$\delta G(s) = K(s)\, \delta P(s) \quad ,$$

with

$$\delta G(s) = \left[G\delta_{q_1}(s) \quad L \quad G\delta_{qn_a}(s) \quad G\delta\rho^*_{Te1}(s) \quad L \quad G\delta\rho^*_{Tenb}(s) \right]^T \quad .$$

As in the previous section, the kernel K(s) could be identified from power modulation experiments around the target steady state, but for the proof of principle experiments that are described in this article, the steady state gain matrix K(0) was sufficient. It was deduced from simple step power changes in dedicated open loop experiments. A PI controller that minimizes the integral least square difference between the requested profiles (defined by Galerkin coefficients δG_{target}), and the profiles that are obtained in steady state [defined by $\delta G(s = 0)$] can be designed by calculating a particular pseudo-inverse K_{inv} of K(0) [67]. This is not immediate because the matrix K(0) is not square and, therefore, an infinite number of possible pseudo-inverse matrices exist. The calculation of the relevant one requires the definition of a positive definite scaling matrix B that contains all the necessary information about the distributed nature of the profiles and is of course directly related to the choice of the basis functions. It takes the block diagonal form:

$$B = \begin{pmatrix} Bq & 0 \\ 0 & \mu B_{\rho^*_{T_e}} \end{pmatrix} . \qquad (11)$$

The general elements (i, j) of the matrices Bq and $B\rho^*_{T_e}$ contain the scalar product of the basis functions and take the form:

$$[B_q]_{i,j} = \int_0^1 a_i(x)\, a_j(x)\, dx \quad \text{and} \quad [B_{\rho^*_{T_e}}]_{i,j} = \int_0^1 b_i(x)\, b_j(x)\, dx \quad ,$$

and μ is a constant scaling parameter (chosen equal to 104) that is used to treat q(x) (of order 1) and $\rho^*_{T_e}(x)$ (of order 0.01) on the same footing in the minimization while allowing more or less weight to be given to the control of one profile or the other. Then, as shown in Ref. [67], a singular value decomposition of the matrix $\hat{K} = \Delta K(0)$, where Δ comes from the Cholesky decomposition of **B** ($B=\Delta^T\Delta$), leads to the construction of K_{inv}.

SIMULTANEOUS CONTROL OF CURRENT AND TEMPERATURE GRADIENT PROFILES IN JET

The real-time controller described above was used experimentally to control the current density

and electron temperature gradient profiles $\rho^*_{T_e}(x)$ and obtain an ITB at about half plasma radius. The current density profile was actually controlled via $\iota(x)$ because, being directly proportional to the total current in [0, x] (sidebar S20), it depends more linearly on the applied current drive power than q(x). To prevent overloading the real-time controller computation, the number of trial basis functions and the radial windows on which they operated were deliberately limited (only part of the full profiles were controlled). The accuracy of the real-time reconstruction of the q-profile from polarimetry data [66] was poor in the central region [$0 < x < 0.2$] so this region was excluded from the control window. In addition, the q-value at the edge is inversely proportional to the total plasma current (sidebar S20), which is accurately controlled by the primary (ohmic) circuit of the tokamak (sidebar S13). Therefore, including the edge region in the q-profile control would have been redundant. Thus, the feedback control of the q-profile was restricted to the region $0.2 \leq x \leq 0.8$. For $\rho^*_{T_e}$, the region of control of the ITB was imposed by limitations in the real-time electron temperature measurements given by the electron cyclotron emission diagnostic, which provides no measurement in the core of the plasma, nor near the edge in discharges with LHCD. The radial measurement window depends on the plasma configuration but includes in all cases the region that extends from x= 0.3 to x= 0.7. Moreover , one of the goals of these experiments was to sustain an ITB at x> 0.4 in order to enhance the plasma performance while q-profiles that are accessible with the present heating systems on JET do not in general allow stationary ITBs at $x \geq 0.6$ to be sustained. Thus, in these experiments the control region for was restricted to the window $0.4 \leq x \leq 0.6$ where an ITB was expected and requested. The Galerkin coefficients of both profiles (five coefficients for ι and three for $\rho^*_{T_e}$) were computed in real-time from the profile measurements and a power request was sent every 10ms by the controller to the different actuators according to Eq.(10). The control scheme was applied in multiple plasma discharges for a maximum of 7 seconds per discharge and successfully reached several different target q-profiles — from monotonic to reversed shear— while simultaneously controlling the profile of the electron temperature gradient . Figure25 shows the result of applying the control algorithm in the case of a monotonic q-profile target and of a $\rho^*_{T_e}$-profile target with a maximum slightly above the criterion in Eq.(8) for the existence of an ITB, at a fairly large radial location (x=0.5) where ITBs are not easily achieved spontaneously. Both profiles are satisfactorily controlled and the effect of the control can be clearly seen in Fig.26. In this example, the ICRH system failed to deliver the requested power at around t= 10.25s, and therefore the control phase was limited to 4.8s.

As mentioned in the previous section, the controller defined by Eq.(10) minimizes, in the integral least square sense, the difference between the target ι and $\rho^*_{T_e}$ profiles and their respective real-time measurements or, more precisely, the quadratic expression

$$dy^2 = \int_{0.2}^{0.8} [\iota(x) - \iota_{setpoint}(x)]^2 \, dx + \mu \int_{0.4}^{0.6} [\rho^*_T(x) - \rho^*_{T_{setpoint}}(x)]^2 dx$$

where μ is a scalar used for relative weighting of the control objectives [Eq.(11)]. This positive definite quantity, which will be referred to as the squared distance between the achieved and requested

profiles, is plotted in Fig.27. An important feature is the increase of this distance in response to the sudden, undesired, failure of the ICRH system to deliver the requested power at t= 10.25s. This failure is indeed immediately followed by a strong rise of the $\rho^*_{T_e}$ contribution to the distance to be minimized, showing, by contrast, the effectiveness of the control before the failure of the actuator.

FUTURE DIRECTIONS

The present controllers were designed using only knowledge of the static linear response model, K(0), but the experimental identification and use of a fully dynamic linear model, K(s), is now under investigation in order to possibly construct a two-time-scale model (resistive diffusion time for current or q-profile evolution and energy confinement time for temperature or pressure profile evolution) and design a controller that can better cope with fast plasma perturbations (MHD events, spontaneous emergence or collapse of ITBs) while converging slowly towards the requested high performance plasma state. Models based on physics (instead of identified from data) could also be used in future devices to identify adequate linear, or piecewise-linear, response matrices. Present state state-of-the-art plasma transport physics modeling is not yet accurate enough to do so (especially in transient regimes), although it can be quite useful for a qualitative assessment of the control algorithms [72].

ACKNOWLEDGEMENTS

Work supported by the U.S. Department of Energy under Contract Nos. DE-FC02-04ER54698, DE-AC02-76CH03073 and Grant No. DE-FG02-92ER54141 and performed under the European Fusion Development Agreement (EFDA). We would like to thank M. Chance, M.S. Chu, and A.D. Turnbull for eddy current figures, M. Leuer for Fig.11, and P.B. Snyder for Fig.9.

REFERENCES

[1]. Z. Chang, et al., "Observation of nonlinear neoclasical pressure-gradient-driven tearing modes," *Phys. Rev. Lett.*, vol. **74** p. 4663, 1995.

[2]. R.J. Buttery, et al., "Onset of neoclassical tearing modes on JET," *Nucl. Fusion*, vol. **43**, p. 69, 2003.

[3]. D.P. Brennan, et al., "A Mechanism for Tearing Onset Near Ideal Stability Boundaries," *Phys. Plasmas*, vol. **10**, p. 1643, 2003.

[4]. R.J. Lahaye, et al., "Control of Neoclassical Tearing Modes in DIII–D," *Phys. Plasmas*, vol. **9**, p. 2051, 2002.

[5]. R.W. Callis, et al., "3MW, 110GHz ECH system for the DIII–D tokamak," *in Proc. 20th Symp. on Fusion Technol., Marseille, France, 1998* (Association EURATOM-CEA, Saint-Paul-Lez-Durance, 1999) vol. **1**, p. 315.

[6]. K. Nagasaki, et al., "Stabilization Effect of Early ECCD on a Neoclassical Tearing Mode in the JT-60U Tokamak," *Nucl. Fusion*, vol. **43**, p. L7, 2003.

[7]. M. Porkolab, “Review of RF Heating,” in Theory of magnetically confined plasmas, Proc. Int. School of Plasma Physics, Varenna, 1977, p. 339, Pergamon Press, Oxford (1979).

[8]. R.J. Lahaye, et al., “Complete Suppression of the m/n=2/1 Neoclassical Tearing Mode Using Radially Localized Electron Cyclotron Current Drive on DIII–D and the Requirements for ITER,” in *Proc. 30th EPS Conf. on Contr. Fusion and Plasma Phys.*, St.Petersbur g, Russia, 2003, vol. **27A**, P-2.109.

[9]. B.W. Rice, “q-profile measurements with the motional Stark effect diagnostic in the DIII–D tokamak,” *Fus. Eng. and Design*, vol. **34-35**, pp. 135-142, 1997.

[10]. ITER [FEAT] Final Design Report (FDR), Plant Description Documents, Chapter 5, Safety, (http://web.gat.com/iter-fdr/final-report-sep-2001/Plant_Descptn_Docs_(PDDs)/PDD_5_Safety.pdf).

[11]. ITER [FEAT] Final Design Report (FDR), Plant Description Documents, Chapter 3, Section 7, Control, (http://web.gat.com/iter-fdr/final-report-sep-2001/Plant_Descptn_Docs_(PDDs)/PDD_3.7_Control.pdf)

[12]. D. Wróblewski, G.L. Jahns, J.A. Leuer, “Tokamak disruption alarm based on a neural network model of the high-β limit,” *Nuclear Fusion*, vol. **37**, p. 725, 1997.

[13]. M.K. Zedda, et al., “Disruption classification at JET with neural techniques,” in *Proc. 30th EPS Conf. on Controlled Fusion and Plasma Physics*, St. Petersburg, Russia, 2003, ECA, vol. **27A**, P-2.93.

[14]. G. Pautasso, et al., “On-line prediction and mitigation of disruptions in ASDEX Upgrade,” *Nucl. Fusion*, vol. **42**, p. 100, 2002.

[15]. F.C. Morabito, et al., “Fuzzi-Neural approaches to the prediction of disruptions in ASDEX-Upgrade,” *Nucl. Fusion*, vol. 40, p. 1715, 2001.

[16]. S.C. Jardin, et al., “A fast shutdown technique for large tokamaks,” *Nucl. Fusion*, vol. **40**, p. 923, 2000.

[17]. D.G. Whyte, et al., “Mitigation of tokamak disruptions using high-pressure gas injection,” *Phys. Rev. Lett.*, vol. **89**, p. 055001/1, 2002.

[18]. P.M. Frank, “Fault diagnosis in dynamic systems using analytical and knowledge-based redundancy—a survey and some new results,” *Automatic*a, vol. **26**, p. 459, 1990.

[19]. R. Isserman and P. Balle, “Trends in the application of model-based fault detection and diagnosis of technical processes,” *Control Eng. Practice*, vol. **5**, p. 709, 1997.

[20]. A. Rizzo, M.G. Xibilia, “An innovative intelligent system for sensor validation in tokamak machines,” *IEEE Transactions on Control Systems Technology*, vol. **10**, p. 421, 2002.

[21]. L. Fortuna, et al., “A neural networks based system for post pulse fault detection and disruption data validation in tokamak machines,” in *Proc. 1999 IEEE Int. Symp. on Circuits and Systems*, VLSI, vol. **5**, p. 563, 1999.

[22]. M.L. Walker, et al., “Automated fault detection for DIII–D tokamak experiments,” in *Proc. 18th IEEE/NPSS Symp. on Fusion Engineering*, Piscataway, New Jersey, p. 539, 1999.

[23]. J.C. Giarratano, G. Riley, “Expert systems principles and programming,” PWS Pub. Co.

[24]. E. Jotaki and S. Itoh, “A data acquisition method against unpredictable events during long-time discharges and its application to the TRIAM-1M tokamak experiment,” *Fusion Tech.*, vol. **32**, p. 487, 1997.

[25]. K. Blackler and A.W. Edwards, “The JET fast central acquisition and trigger system,””*JET Report*, JET-P(93) 49, 1993.

[26]. V. Mertens, G. Raupp, and W. Treutterer, “Plasma control in ASDEX Upgrade,””*Fusion Sci. and Tech.*, vol. **44**, p. 593, 2003.

[27]. H. Zohm, “Edge localized modes (ELMs),””*Plasma Phys. Control. Fusion*, vol. **38**, pp. 105-128, 1996.

[28]. R.J. Groebner, “An emerging understanding of H–mode discharges in tokamaks,””*Phys. Fluids B*, vol. **5**, p. 2343, 1993.

[29]. G. Federici, et al., “Assessment of erosion of the ITER divertor targets during type I ELMs,” Plasma Phys. Control. Fusion vol. **45**, pp. 1523-1547, 2003.

[30]. P.B. Snyder, et al., “Progress in the Peeling-Ballooning Model of ELMs: Toroidal Rotation and 3D Nonlinear Dynamics,” 31st EPS Conference on Plasma Physics, London UK, June 2004

[31]. P.T. Lang, “Active edge localized mode (ELM) frequency control with pellets,” in *Proc. 30th EPS Conf. on Contr. Fusion and Plasma Phys.*, St. Petersburg, Russia, 2003, ECA vol. **27A**, p. 1.129.

[32]. A.W. Degeling, “Magnetic triggering of ELMs in TCV,” in *Proc. 30th EPS Conf. on Contr. Fusion and Plasma Phys.*, St. Petersburg, Russia, 2003, ECA.

[33]. M. Greenwald, et al., “Studies of EDA H–mode in Alcator C–Mod,” *Plasma Phys. Control. Fusion*, vol. **42**, pp. A263-A269, 2000.

[34]. K. Kamiya, et al., “Observation of high recycling steady H-mode edge and compatibility with improved core confinement mode on JFT-2M,” *Nucl. Fusion*, vol. **43**, pp. 1214–1219, 2003.

[35]. K.H. Burrell, et al., “Quiescent H–mode plasmas in the DIII–D tokamak,” *Plasma Phys. Control. Fusion*, vol. **44**, pp. A253-A263, 2002.

[36]. K.H. Burrell, et al., “Quiescent double barrier H–Mode plasmas in the DIII–D tokamak,” *Phys. Plasmas*, vol. **8**, p. 2153, 2002.

[37]. W. Suttrop, et al., “Stationary ELM-free H–mode in ASDEX upgrade,””*Plasma Phys. Control. Fusion*, vol. **46**, p. A151, 2004.

[38]. T.E. Evans, R.A. Moyer, J.G. Watkins, et al., “Suppression of large edge localized modes in high confinement DIII–D plasmas with a stochastic magnetic boundary,” presented at the 16th Int. Conf. on Plasma Surface Interactions, Portland, Maine, 2004 in press, *J. Nucl. Mater.*; and T.E. Evans, R.A. Moyer, P.R. Thomas, et al., *Phys. Rev. Lett.*, vol., **92**, p.235003-1, 2004.

[39]. R. Aymar, et al., “ITER: fusion research at the dawn of a new era,” 19th IAEA Fusion Conference, Lyon, France, October 14-19, 2002, OV/1-1.

[40]. L.C. Bernard, et al., “GATO: An ideal MHD stability code for axisymmetric plasmas with internal separatrices,” *Commun. Comput. Phys.*, vol. **24**, p. 377, 1981.

[41]. T.S. Taylor, et al., “Optimized profiles for improved confinement and stability in the DIII–D tokamak,” *Plasma Phys. Control. Fusion*, vol. **36**, p. B229, 1994.

[42]. M. Okabayashi, et al., “Role of the stabilizing shell in high-beta, low-q disruptions in PBX-M,” *Nucl. Fusion*, vol. **36**, p. 1167, 1996.

[43]. A.M. Garofalo, et al., “Sustained rotational stabilization of DIII–D plasmas above the no-wall beta limit,” *Phys. Plasmas*, vol. **9**, p. 1997, 2002.

[44]. S. Takeji, et al., “Resistive instabilities in reversed shear discharges and wall stabilization on JT-60U,” *Nucl. Fusion*, vol. **42**, p. 5, 2002.

[45]. M. Okabayashi, et al., “Stabilization of the resistive wall mode in DIII–D by plasma rotation and magnetic feedback,” *Plasma Phys. Control. Fusion*, vol. **44**, p. B339, 2002.

[46]. E.J. Strait, et al., “Resistive wall mode stabilization with internal feedback coils in DIII–D,” to be published in *Phys. Plasmas*, 2004.

[47]. M. Okabayashi, N. Pomphrey, R.E. Hatcher, “Circuit equation formulation of resistive wall mode feedback stabilization schemes,” *Nucl. Fusion* vol. **38**, p. 1607, 1998.

[48]. Allen H. Boozer, “Equations for studies of feedback stabilization,” *Phys. Plasmas*, vol. **5**, p.3350, 1998.

[49]. Y.Q. Liu, A. Bondeson, “Active Feedback Stabilization of Toroidal External Modes in Tokamaks,” *Phys. Rev. Lett.*, vol. **84**, p. 907, 2000.

[50]. M.S. Chu, et al., “Modeling of feedback and rotation stabilization of the resistive wall mode in tokamaks,” *Nucl. Fusion*, vol. **43**, pp. 196-201, 2003.

[51]. D.H. Edgell, et al., “Magnetohydrodynamic mode identification from magnetic probe signals via a matched filter method,””*Rev. Sci. Instrum.*, vol. **73**, p. 1761, 2002.

[52]. C.M. Fransson, D.H. Edgell, D.A. Humphreys, M.L. Walker, “Model validation, dynamic edge location mode discrimination, and high confidence resistive wall mode control in DIII–D,”*Phys. Plasmas*, vol.**10**, no.10, pp. 3961-3974, 2003.

[53]. C.M. Fransson, B. Lennartson, C. Breitholtz, A. Bondeson, Y.Q. Liu, “Feedback stabilization of nonaxisymmetric resistive wall modes in tokamaks,” II. Control Analysis, *Phys. Plasmas*, vol. **7**, no.10, pp. 4143-4151, 2000.

[54]. A. Bondeson, et al., “Active feedback stabilization of high beta modes in advanced tokamaks,” *Nucl. Fusion*, vol. **41**, p. 455, 2001.

[55]. M. Okabayashi, et al., “Active feedback stabilization of the resistive wall mode on the DIII–D device,” *Phys. Plasmas*, vol. **8**, p. 2071, 2001.

[56]. J. Bialek, et al., “Modeling of active control of external magnetohydrodynamic instabilities,” *Phys. Plasmas*, vol. **8**, p. 2170, 2001.”

[57]. M.S. Chu, et al., “Modeling of Feedback Stabilization of Resistive Wall Mode in Rotating Plasmas,” *Phys. Plasmas*, vol. **11**, p. 2497, 2004.

[58]. T.S. Taylor, et al., “Physics of advanced tokamaks,” *Plasma Phys. Control. Fusion*, vol. **39**, p. B47, 1997.

[59]. J. Connor et al., “A review of internal transport barrier physics for steady state operation of tokamaks,” *Nucl. Fusion*, vol. **44**, p. R1, 2004.

[60]. F. Wagner, et al., “Regime of improved confinement and high beta in neutral beam heated divertor discharges of the ASDEX tokamak,” *Phys. Rev. Lett.*, vol. **49**, p. 1408, 1982.

[61]. T.J.J. Tala, et al., “ITB formation in terms of flow shear and magnetic shear on JET,” *Plasma Phys. Control. Fusion*, vol. **43**, 507, 2001.

[62]. E. Joffrin, et al., v“Triggering of internal transport barrier in JET,” *Plasma Phys. Control. Fusion*, vol. **44**, p. 1739, 2002.

[63]. X. Garbet, et al., “Micro stability and transport modelling of internal transport barriers on JET,” *Nucl. Fusion*, vol. **43**, p. 975, 2003.

[64]. G. Tresset, et al., “A dimensionless criterion for characterising internal transport barriers in JET,” *Nucl. Fusion*, vol. **42**, p. 520, 2002.

[65]. D. Mazon, et al., “Real-time control of internal transport barriers in JET,” *Plasma Phys. Control. Fusion*, vol. **44**, p. 1087, 2002.

[66]. L. Zabeo, et al., “A versatile method for the real-time determination of the safety factor and density profiles in JET,” *Plasma Phys. Control. Fusion*, vol. **44**, p. 2483, 2002.

[67]. D. Moreau, et al., “Real-time control of the“-profile in JET for steady state advanced tokamak operation,” *Nucl. Fusion*, vol. **43**, p. 870, 2003.

[68]. L. Laborde, et al., “A model-based technique for real-time control of current and pressure profiles in the JET tokamak,” submitted to *Plasma Phys. Control. Fusion*, 2004.

[69]. C.D. Challis, et al., “Effect of“-profile modification by LHCD on internal transport barriers in JET,” *Plasma Phys. Control. Fusion*, vol. **43**, p. 861, 2001.

[70]. X. Litaudon, et al., “Towards fully non-inductive current drive operation in JET,” *Plasma Phys. Control. Fusion*, vol. **44**, p. 1057, 2002.

[71]. E. De la Luna, et al., “Recent developments of ECE diagnostics at JET,” *13th Joint Workshop on ECE and ECRH 2004*, http://www.ec13.iapras.ru/on-line-papers.htm, and E.Jof frin, etal., ‘Integrated scenario in JET using real-time profile control,” *Plasma Phys. Cont. Fusion*, vol. **45**, p. A367, 2003.

[72]. T. Tala, et al., “Progress in transport modelling of internal transport barrier and hybrid scenario plasmas in JET,” submitted to Proc. 20th IAEA Fusion Energy Conference, Vilamoura, Portugal, 2004.

APPENDIX. ADDITIONAL SIDEBARS.

These sidebars will be located in other papers in the same special issue.

S18. TOKAMAK SCENARIOS (SIDEBAR)

The term *scenario* is often used in tokamak plasma physics to refer to a planned sequence of operating points for a particular tokamak device and plasma. The definition of these operating points usually includes specification of a particular sequence of plasma cross-sectional shapes and plasma current values, but it can also include a number of other plasma parameters such as the value of β (sidebar S2) or, more generally, characteristics of plasma profiles (sidebar S5) and other plasma characteristics. Because increasing the performance of the plasma (sidebar S2) tends to also make it more susceptible to instabilities, planning and simulating scenarios to achieve high performance while maintaining plasma controllability is an important part of the work that occurs at the interface between plasma physics and plasma control.

When scenarios are discussed in the context of control, they usually include the evolution of operating points for the actuators that are needed to control desired features of the plasma. This is done for two reasons. Given limitations in actuators, it provides some confidence that a specified sequence of operating points can be produced by the device. It also enables use of feedforward programming of the actuators, which facilitates linear feedback control of the nonlinear plasma system that is linearized around successive operating points. For example, nominal values of the PF coil currents that are predicted to be consistent with a sequence of plasma shapes are sometimes used to define pre-programmed nominal trajectories for these currents or for the voltage actuators driving the PF coils. Scenarios can also include specification of whether and how actuators will be used. For example, a particular heating and current drive actuator (sidebar S13) can be used for either heating or for current drive or not used at all.

The term scenario is not completely well defined in the plasma physics and control literature. It sometimes implies a complete specification of the plasma evolution, and at other times refers only to plasmas having a specific characteristic behavior, such as a particular profile shape. Usually, it is clear from the context which of these meanings is assumed.

S19. TOKAMAK TIMESCALES (SIDEBAR)

The various processes in tokamak plasmas evolve on a number of distinctively different characteristic timescales. These time scales range from less than a microsecond to many seconds. The fastest of these is the so-called *Alfven timescale*, which refers to the growth time of those MHD (sidebar S3) instabilities that have no passive stabilizing effects (the *Alfven instabilities* or *Alfven eigenmodes*). This timescale is also referred to as the *ideal MHD timescale* and the instabilities as *ideal MHD instabilities*. For example, the vertical displacement instability of a vertically elongated plasma (sidebar S6) would have a growth time of a few microseconds or less were it not for the stabilizing influence of induced *eddy currents* in passive conducting structures (sidebar S17). When partially

stabilized by induced currents in passive conductors, ideal MHD instabilities are converted to instabilities that grow on a time scale determined by the time needed for the induced currents to decay away due to conductor resistance. This time scale is sometimes called the *wall time* or *resistive wall time*. On present day devices, this is usually on the order of a few milliseconds but can vary considerably since it is determined by the resistance and inductance of the set of conducting elements in the device.

Other important timescales include the times required for evolution of transport quantities (density, temperature, and pressure profiles) and for evolution of the current profile (sidebar S20). In general, the current profile requires a much longer time to evolve (on the order of 5 or 10 times greater) than the transport quantities. Characteristic timescales are often known by more than one label, which can be a bit confusing. For example, *transport timescales* are also known as *confinement timescales*. Terms used for several similar current profile evolution characteristic times include the *(global) resistive diffusion time, current diffusion time, skin time*, or *current relaxation time*, the multiple names reflecting different characterizations of the physical processes that define the evolution. Although there are a number of other tokamak process timescales, those described above are the most relevant to the discussions in this special issue.

The issue of characteristic time scale is an important one for tokamak control. For example, an unstable process with a fast time scale stresses the importance of fast real time control calculations and actions. This is why the control of the relatively fast and low dimensional plasma vertical instability is usually performed separately from the slower, high dimensional plasma boundary shape control.

Control experiments must also run for a length of time sufficient to judge the effectiveness of new control methods. A primary goal of almost all tokamak control is the maintenance of some performance objective in steady state conditions. The precise length of time that defines a steady state evaluation is not universally agreed upon, but it clearly must have a length equivalent to multiple characteristic times of the process under control. As more control integration takes place, a significant challenge is to combine controls operating on the many different time scales.

S20. PROFILES (SIDEBAR)

A number of relationships between several plasma profiles (sidebar S5) are used in this article. We describe some of these relationships here in order to switch easily from one to another in the discussion. The safety factor (q) profile was defined in sidebar S5. An alternate definition is given by

$$q(\rho) = \oint \frac{1}{R} \frac{B_\phi}{B_p} \, ds \quad ,$$

where β_ϕ is the toroidal field (field in the direction of the toroidal coordinate ϕ; see Fig.12 of the intro article), β_p is the poloidal field (field in the (R,Z) plane orthogonal to the coordinate ϕ), and

the integration is carried out over a single poloidal circuit around the flux surface corresponding to the normalized flux value ρ (sidebar S5) [Wesson]. This is one of the definitions for q that indicates why q is considered a measure of magnetic pitch. The toroidal field β_ϕ is dominated by the contribution from the toroidal field coils (see Fig.5 of the intro article), which are typically operated so as to produce an approximately constant (in time) toroidal field. Thus, in most experiments, the safety factor profile is considered to be primarily a function (in time) of the variable poloidal component of the magnetic field. The poloidal field β_p is produced by toroidal currents, including the current in the plasma and current in the poloidal field (PF) coils. When the plasma shape is controlled at a steady state equilibrium, the PF coil currents are nearly constant, so changes in poloidal field are dominated by changes in the spatial distribution of plasma toroidal current density (the *current profile*). Through this chain of dependencies, it can be seen that the safety factor profile depends on the current profile (and vice versa). Thus, many physicists speak interchangeably of control of the current profile and of the q-profile.

A quantity known as the local *magnetic shear* is proportional to the spatial derivative of the safety factor, $s(\rho) \propto dq/d\rho$. Magnetic shear plays a role in plasma stability, but in this article (and in much of the literature) it is used simply as an alternative description for the behavior of the q-profile. In particular, the notion of *negative (central) shear*, also known as *reverse shear*, describes a q-profile that is not monotonic (Fig.A-1). Another quantity related to q is the inverse of the safety factor known as iota, $\iota(\rho) = 2\pi/q(\rho)$. It can be shown that $\iota(\rho)$ is proportional to the total current inside the flux surface represented by the normalized flux value ρ. In particular, this means that the value $\iota(1) = 1/q(1)$ at the edge of the plasma is inversely proportional to the total plasma current. The q-, s-, and iota-profiles, are all functions of normalized flux ρ, while the current profile is not. The current profile is typically defined as the plasma current density along a line extending radially from the magnetic axis to the plasma edge (Fig.14 of intro).

Type	**W_{PED}**	**DW_{ELM}**	**df_{ELM}/dP**	**Density**	**Shaping**
I	1	$0.05–0.25W_{PED}$	> 0	1	Any
II	1	$< 0.01W_{PED}$	< 0	» 1	Strong
III	< 2/3	$< 0.01W_{PED}$	< 0	» 1 or « 1	Any

Table 1: Experimental characteristics of different ELM types. The ELM type with the widest operational range, Type I [Fig.7(c)], allows large pressure in the ETB (the pedestal energy W_{PED} = pressure on inside edge of the ETB times the plasma volume) but the energy loss at each ELM, ΔW_{ELM}, is also large. (The symbol W is widely used in plasma physics to denote quantities of energy. Note that pedestal energy is not the same as total stored energy.) The Type II ELM has low ELM energy loss and high ETB pressure but is observed only in a limited range of plasma shaping and density that may not be applicable to a tokamak reactor. The Type III ELM [Fig.7(a)] has a wider operational range than the Type II and low ELM energy loss but also reduced pressure in the ETB. The pedestal energy and density shown here are values relative to the conditions under which Type I ELMs occur.

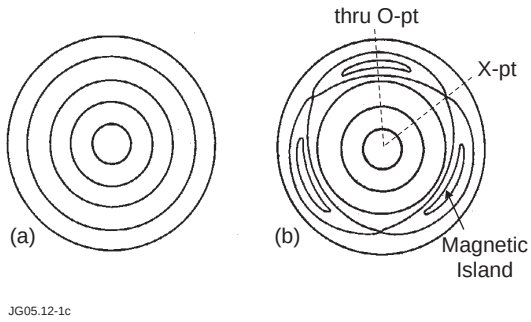

Figure 1: Illustration of magnetic islands topology in a circular cross-section plasma. Perfectly conducting ideal MHD plasmas (sidebar S3) require nested flux surfaces (a), while resistive plasmas can produce tearing and reconnection *(hence the name* tearing mode*) of flux surfaces, resulting in magnetic islands (b). Localized current and pressure profiles (sidebar S5) are flattened across an island (whose center is the* O-point*). The resulting connection between inner and outer island surfaces (joined at the* X-point*) allows heat to leak out of the plasma core faster than it would without the island, thus degrading confinement. (b) shows the island topology corresponding to a 3/2 NTM [periodicity of (sidebar S4) in the poloidal cross section shown, and a periodicity of in the toroidal direction (not illustrated)].*

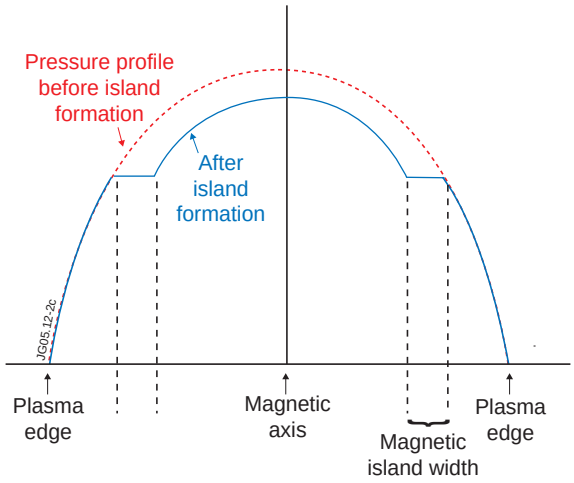

Figure 2: Flattening of the pressure profile caused by the NTM. Islands driven by the NTM are responsible for a lowering of temperature, pressure, and current both on and inside the island.

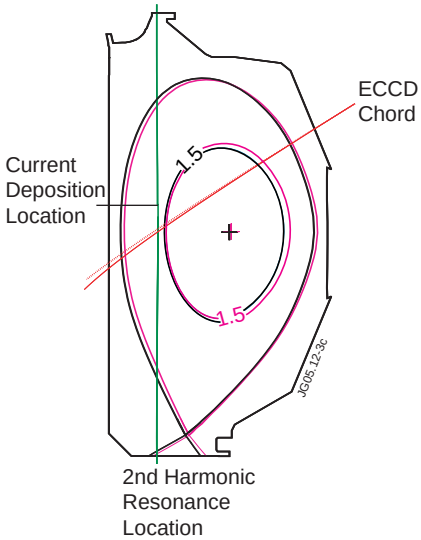

Figure 3: Geometry of current drive to suppress NTM islands. Driving current at the flux surface which contains islands can restore the current lost in island formation. This shrinks and can even eliminate the island, stabilizing the mode. In the case shown, the flux surface (for two different times during the discharge) being affected corresponds to the 3/2 NTM, and is labeled by the safety factor contour value of 1.5. The location where current is actually deposited is slightly offset from the second harmonic resonance due to a Doppler shift.

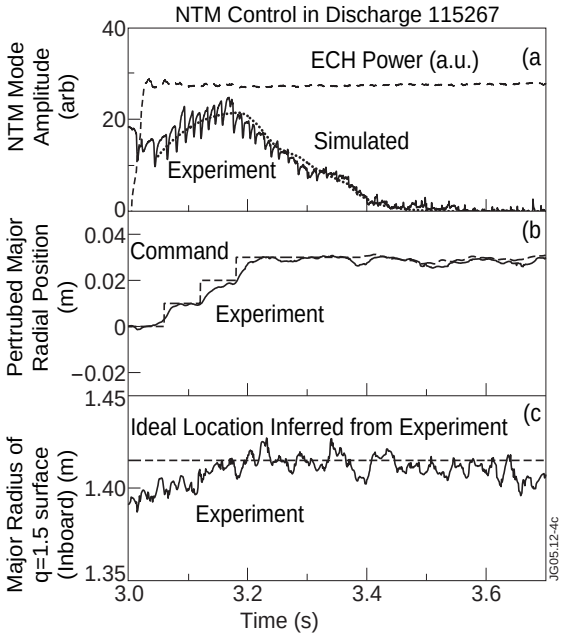

Figure 4: The DIII–D Search and Suppress algorithm with Active Tracking has been successful in suppressing and sustaining stabilization of the NTM. Search and Suppress is engaged at approximately 3.0s and Active Tracking is engaged at approximately 3.4s. (a) Comparison of model predicted and experimental amplitude of the NTM mode (related to the island width), and input ECH power (b) change in the plasma major radius to achieve and maintain alignment between NTM island and ECCD deposition location, (c) major radius of the 3/2 NTM island flux surface (dashed line = empirically determined ECCD deposition location).

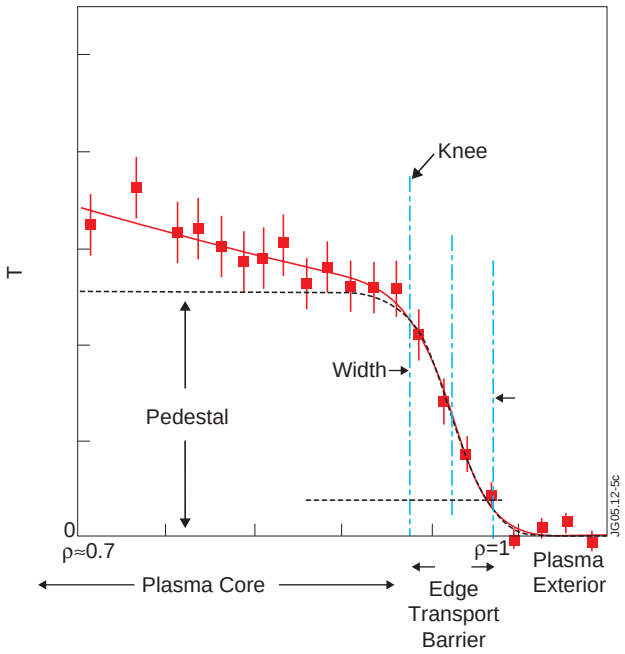

*Figure 5: Illustration of definitions relevant to ELMs. The solid red curve is fitted to measured electron temperature data. Lines through the data points indicate plus or minus one standard deviation (estimated) from measurements. The–*edge transport barrier *(ETB) is a region at the edge of the plasma that is a barrier to the* transport *(diffusion) of heat and particles out of the plasma. The ETB and other forms of transport barrier are characteristic of high energy confinement mode (H–mode) plasmas, since they tend to prevent heat from escaping the plasma. Width of the ETB is defined to be the width of the steep gradient region in the electron temperature profile. This edge region is defined to be the region between the knee of the fitting function and the plasma last closed flux surface. The* pedestal *in temperature coincides with the plasma interior region. (Unfortunately, terminology in the literature is inconsistent, with "pedestal" sometimes being used to refer to the edge region.) The pressure profile in H–mode plasmas takes a similar form, so in discussions of edge transport barriers, temperature and pressure are often used interchangeably. However, pressure can sometimes have a narrower steep gradient region. The close proximity of the high pressure region inside the ETB and the low pressure region outside the ETB is the source of the ELM instability.*

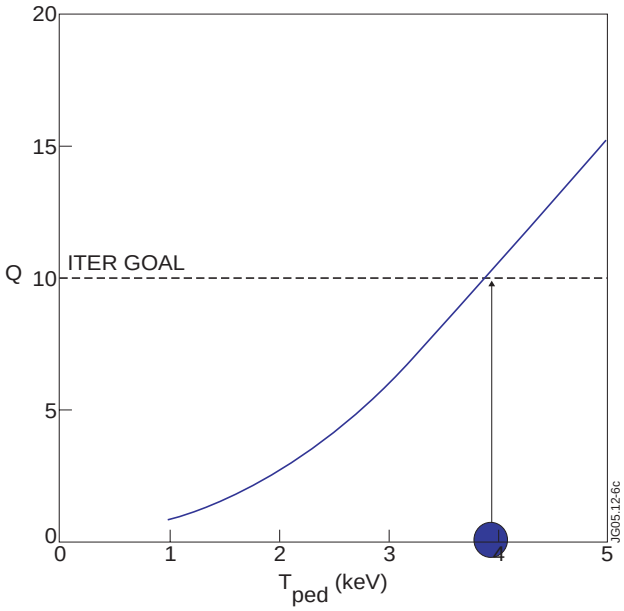

Figure 6: Plot of projected dependence of Q on pedestal temperature. Q is the ratio of fusion power output to additional heating power into the plasma and is a measure of efficiency of fusion power production. This plot assumes fixed available input power (40MW) and constant density across the pedestal (Fig.5). The pedestal temperature must be maintained at approximately 4keV (4 thousand electron volts) in order to sustain the ITER minimum value of Q = 10.

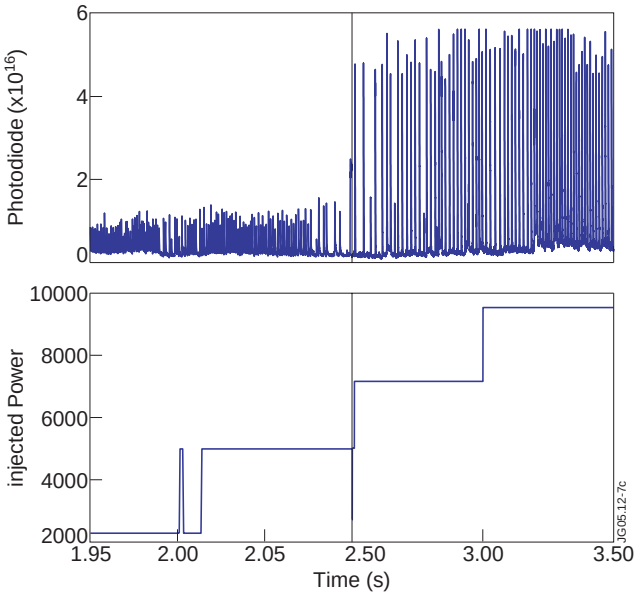

Figure 7: Illustration of different ELM types' dependence on injected power. (a) Detected light emission for Type III ELMs, (b) neutral beam power injected into the plasma simultaneous with measurement (a), (c) detected light emission for Type I ELMs, (d) neutral beam power injected into plasma simultaneous with (c). One characteristic which distinguishes Type I and Type III ELMs is their response to increases in injected power. The frequency of Type I ELMs increases with increasing power while the frequency of Type III decreases. Another characteristic is the typically much larger peak amplitude of Type I ELM light emissions.

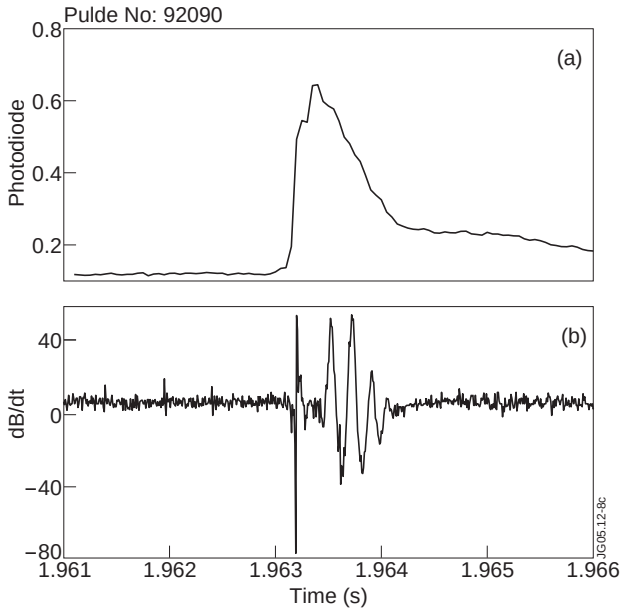

Figure 8: Illustration of the magnetic character of an ELM. (a) Expansion of a single instability similar to those shown in Fig. 7(c); (b) measurement of the derivative of magnetic field at the outboard midplane showing magnetic behavior simultaneous with the light emission in (a).

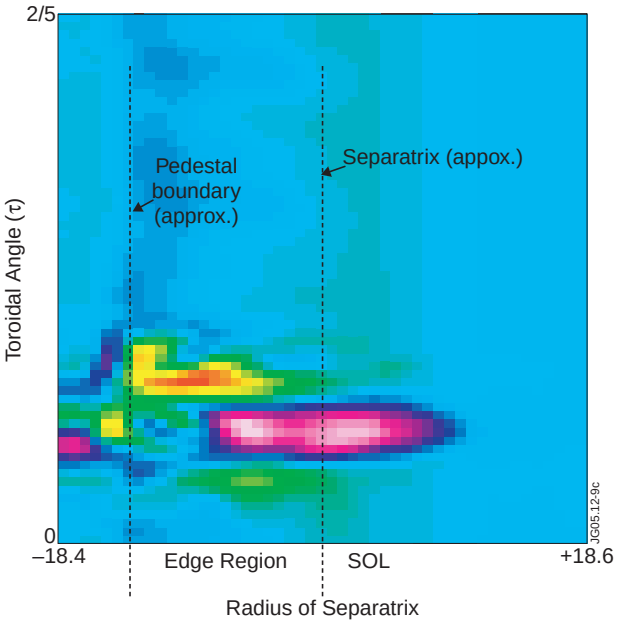

Figure 9: Intensity plot of perturbed density at the plasma outer midplane during the later nonlinear phase of simulation of the growth of the edge localized mode. The early phase of the mode growth is linear and approximately represented by ideal MHD. The local nature of the mode growth is illustrated with the "finger" of plasma radiating out from the plasma edge and toward the vacuum vessel wall. It also extends along the magnetic field (into and out of the page). Large transport through the walls of the finger or possibly the breaking off (magnetic reconnection) of the finger are possible mechanisms for the ELM energy loss.

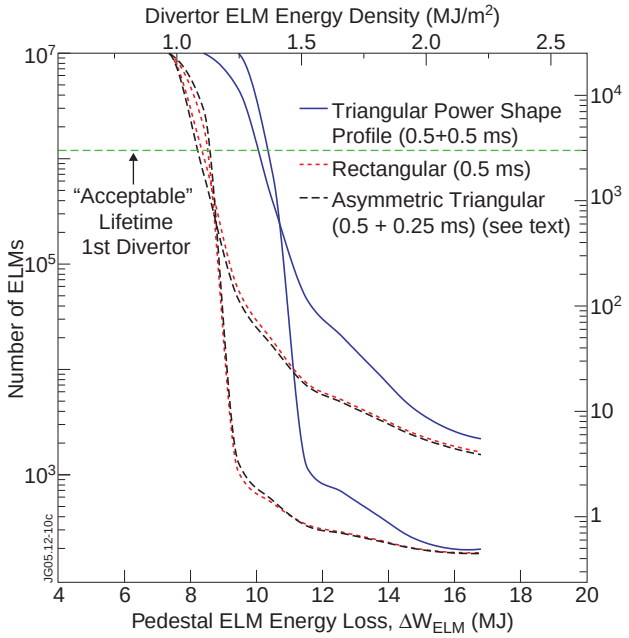

Figure 10: Expected erosion lifetime of ITER divertor plasma facing components (expressed in terms of number of ELMs or corresponding ITER full power pulses) as a function of ELM energy loss from the pedestal, ΔW_{ELM} (see Table 1). Curves are shown for two possible materials — carbon fiber composites (CFC) and tungsten (W) — and for three different approximations to the power signal during an ELM. The lifetime of the ITER divertor (sidebar S9) drops quickly as the energy lost per ELM increases. Uncertainties in extrapolating expected ELM energies from present devices make it difficult to know precisely what to expect in the ITER device. (Reproduced from Ref.29 by permission of G. Federici and the Institute of Physics).

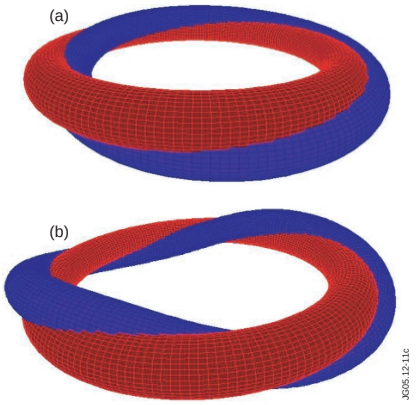

Figure 11: Illustration of kink deformations of a circular cross-section plasma (greatly exaggerated for illustration). The red torus represents a circular cross-section plasma before deformation. The blue surface represents the deformed plasma. (a) an kink. (b) an kink, in which the plasma perturbation repeats itself twice as the toroidal angle varies from 0 to 2π. In each case, the deformation follows a helical path with respect to the undeformed plasma.

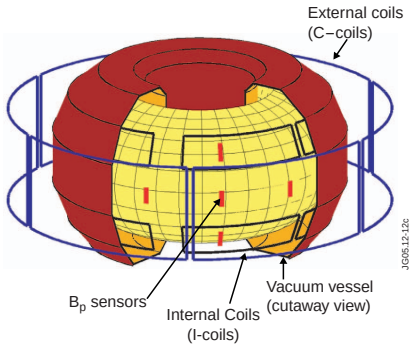

Figure 12: RWM real time control sensors and actuators currently installed on the DIII–D device. The vacuum vessel (represented by the brown surface) is cut away to show internal detail. The plasma is represented by a yellow surface.–Sensors: Typical sensors for radial flux measurement are provided by window frame shaped saddle loops (sidebar approximately concentric with those coils; they are also known as radial flux loops. Radial flux is the same as the integral of radially directed magnetic field (B_r) normal to the wall over a broad area, $\psi = \int_{A_1} B_r dA$, where is the area subtended by the loop. Although, strictly speaking, these saddle loops measure radial flux, measurements made by these sensors are often referred to as radial field measurements because of this integral relationship between field and flux. The poloidal field (B_p) sensors (red) are magnetic probes (sidebar S7). These sensors are mounted on the vessel wall and measure the local magnetic field component tangent to the wall. Actuators: The C-coil set (blue rectangles) consists of six coils located on the midplane outside the vacuum vessel. The I-coil set (black rectangles) inside the vessel consists of two sets of six coils at upper and lower off-midplane angles, installed between the vacuum vessel wall and the plasma-facing carbon tiles.

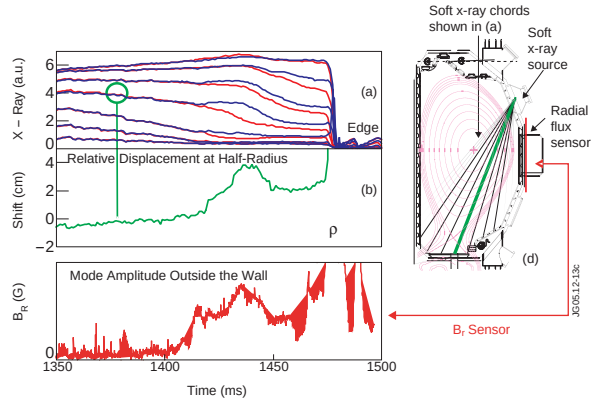

Figure 13: Observation of an RWM inside a plasma by the soft x-ray diagnostic and outside the vacuum vessel by a magnetic sensor: (a) time-dependent measurements of soft x-ray data measured at two toroidal locations (red and blue) spaced 150 deg apart (a.u. = arbitrary units). These measurements can be used to estimate plasma fluid displacement. (b) displacement of the plasma fluid corresponding to the soft x-ray line circled in (a). (c) amplitude of the radial magnetic field measured just outside the vessel during this time. Note the strong correlation between the fluid displacement in (b) and magnetic field growth in (c). (d) DIII–D cross section showing the soft x-ray and magnetic field measurement locations. The thick green soft x-ray chord corresponds to the signal shown in (b). The helical n = 1 internal mode structure is observable as differences in displacement measured by the two soft x-ray arrays (a) which are separated by 150 deg in the toroidal direction. The soft x-ray diagnostic detects the x-rays emitted by a residual amount of impurity ions caused by electron bombardment. This diagnostic is not sufficiently robust for real time use, since the signals are also sensitive to minor changes of other plasma properties.

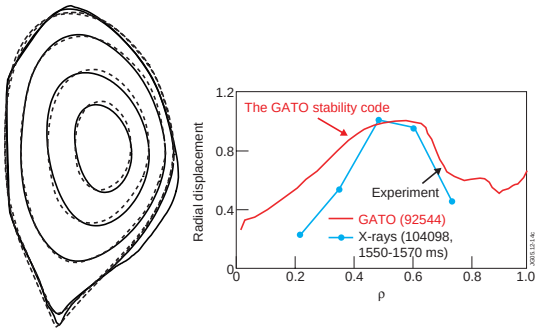

Figure 14: Comparison of theoretically predicted RWM structure with measurement. (a) Structure of the RWM displacement from the axisymmetric plasma as computed by the GATO ideal MHD code [40]. The dashed lines represent constant flux surfaces before deformation. Solid lines represent these flux surfaces after deformation by the RWM. Perturbations are greater at larger radii R because of the inverse dependence of the confining field on radius. The displacement magnitude is exaggerated for illustration. (b) A comparison of the experimental plasma fluid radial displacement estimated using soft x-ray data (see Fig.3) and the mode radial displacement predicted by GATO. The magnitude is normalized to the maximum amplitude (about 8cm) near ρ = 0.5. (The normalized flux coordinate was ρ defined in sidebar S5.) The prediction accuracy is adequate for control, at least in the region where there is data for comparison.

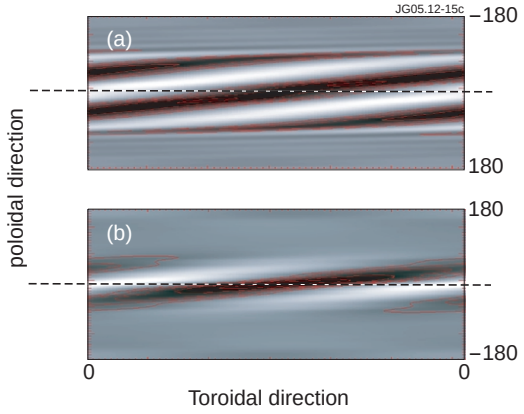

Figure 15: Normal field perturbation on the plasma surface due to an RWM as calculated with the GATO ideal MHD code [40]. Perturbations are relative to the normally axisymmetric (independent of toroidal angle) values that occur in the absence of an RWM. (a)Per turbed normal field at the plasma surface due to plasma current, (b) perturbed normal field at the plasma due to the wall currents. A poloidal angle of 0 corresponds to the outer midplane (see Fig.12 of intro). The normal fields shown reflect the pattern of current flow in the two conducting surfaces. Lighter colors are more positive, darker more negative. The eddy current on the wall is induced by perturbations of the plasma surface current as discussed in the text. The plasma surface current is maximum at the outer midplane and decreases rapidly toward the inner-major radius side. Correspondingly, the eddy current on the wall is maximum at the major radius side since it is inductively coupled. Note that the pattern is periodic with toroidal period one (mode number n = 1), and that the high and low amplitudes in the mode wind their way in a helical pattern around the torus.

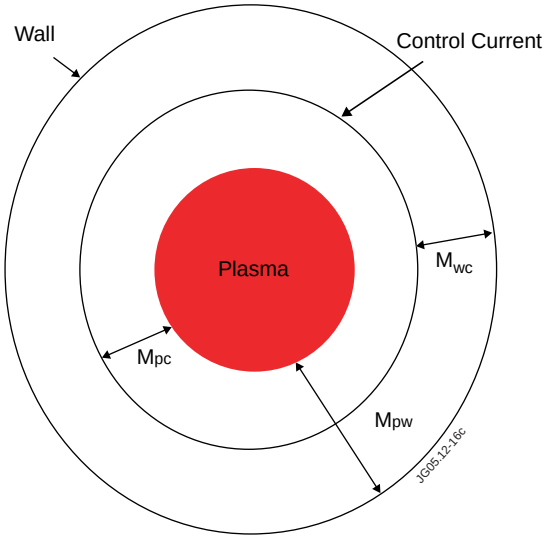

Figure 16: Cross section of cylindrical model of RWM dynamics. The model shown represents the case where the control coils are inside of the vessel wall. The interaction between current in the plasma, wall, and control coils (subscripts p, w, and c) is determined by the mutual inductance values M. Drawing is not to scale.

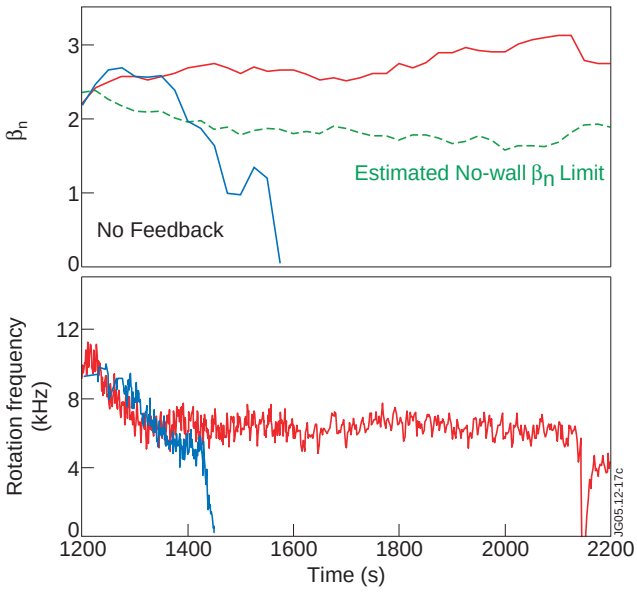

Figure 17: Demonstration of supression of the RWM instability through plasma rotation. As long as plasma rotation remains above a critical frequency (red curve, bottom) of about 6kHz, the mode remains stabilized, even for plasma beta well above the no-wall limit (red curve, top). If plasma rotation falls below the critical value (blue curve, bottom), the mode becomes unstable, causing loss of plasma pressure (blue curve, top), accelerated slowing of the rotation, and shortly thereafter, loss of the plasma to the unstable mode.

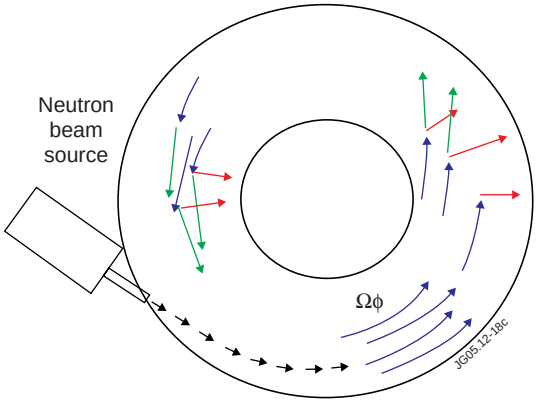

Figure 18: Illustration (top view) of one proposed model of the effect of toroidal rotation on the RWM. In a toroidally rotating plasma, individual particles flow with an average speed defined by the bulk fluid rotation frequency Ω_ϕ. An n = 1 RWM causes the plasma fluid to "bulge" radially outward on one side of the torus and inward at a location 180deg opposite (see Fig.1). Individual particles driven by the RWM and the component of their velocity vectors induced by the RWM are indicated in red. Continually flowing particles with toroidal momentum (blue arrows) frequently collide with the RWM driven particles and impart some of their momentum. The resulting velocity (green arrows) of the originally radially directed particles have significant toroidal components.

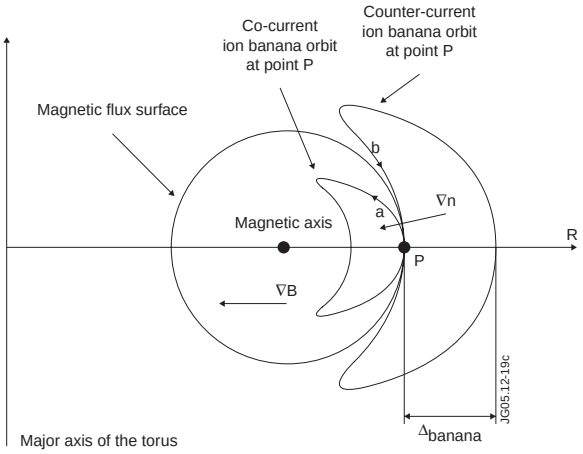

Figure 19: Poloidal projection of two different trapped particle trajectories *(also called* banana orbits*) passing through a point P in the low-field (outer radial) side of the tokamak equatorial plane. (The particle trajectories also extend a long way in the toroidal direction around the major axis of the torus when moving from the bottom turning point to the top one.) The magnetic flux surface passing through the same point is also represented. Trajectory (a) corresponds to an ion that would move toroidally in the co-current direction when passing through point P, whereas trajectory (b) corresponds to an ion that would move toroidally in the counter-current direction at the same location. Due to the density gradient (increasing density towards the center of the plasma), there are more ions with type (a) orbits than ions with type (b) orbits and an anisotropic velocity distribution is sustained at point P.*

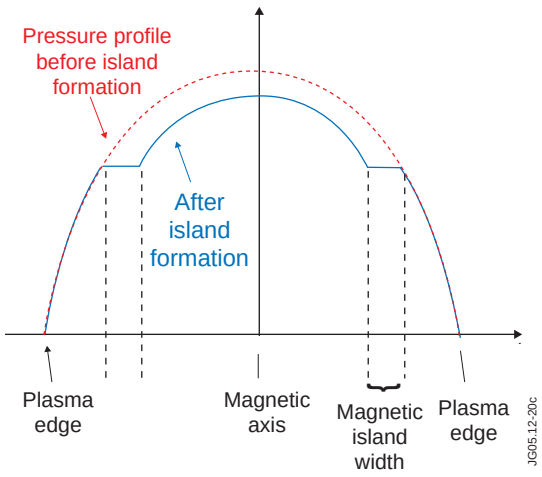

Figure 20: From Ref. 65. Control of an ITB with two Single input-Single output feedback loops. The top two frames show the plasma current, I_p, and the LHCD, NBI and ICRH heating powers. The values of the maximum normalised electron temperature gradient, $max[\rho^*_{T_e}]$ (fourth frame), and of the neutron production rate, R_{NT} (third frame), are maintained close to their setpoints, using ICRH and NBI as actuators respectively. Control starts at 4.5s and the setpoint values are 0.025 for $max[\rho^*_{T_e}]$ and 0.9×10^{16} neutron/s for the neutron production rate. The control of the ITB is sustained for 7.5s. During the whole period of time when the control is applied the loop voltage, V_s (bottom frame), is close to zero, implying that the current is entirely driven by non-inductive sources (sidebar S13) including the self-generated bootstrap current (sidebar S15). The LHCD power is kept approximately constant (≈ 3MW) during the whole control phase to slow down the q-profile relaxation.

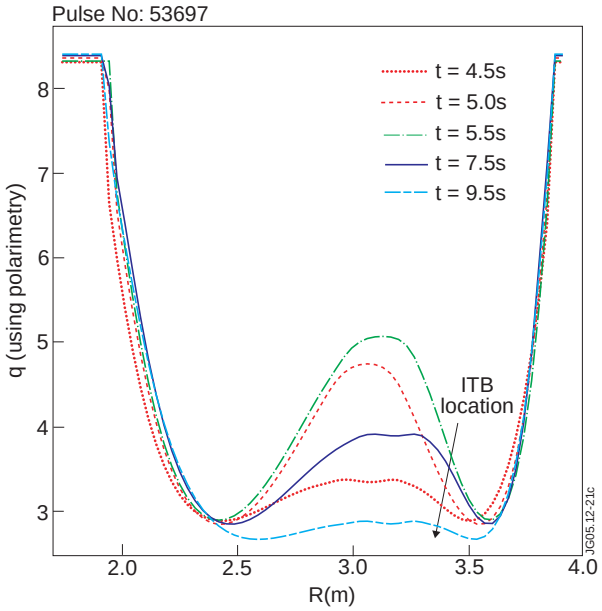

Figure 21: From Ref.65. Illustration of the current diffusion process. Time evolution of the -profile as calculated from a magnetic equilibrium reconstruction code, constrained by polarimetry data, with LHCD held constant (≈3MW) during the high power heating phase. The figure shows that the q-profile evolution is slow, and in particular that the minimum value of q is almost frozen, with a direct effect on the ITB evolution which is practically stationary around R= 3.4m wher e q ≈ 3 and the magnetic shear is negative. Nevertheless, the current profile continues to evolve slowly and this simple ITB control could not be extended to pulse durations longer than the resistive time.

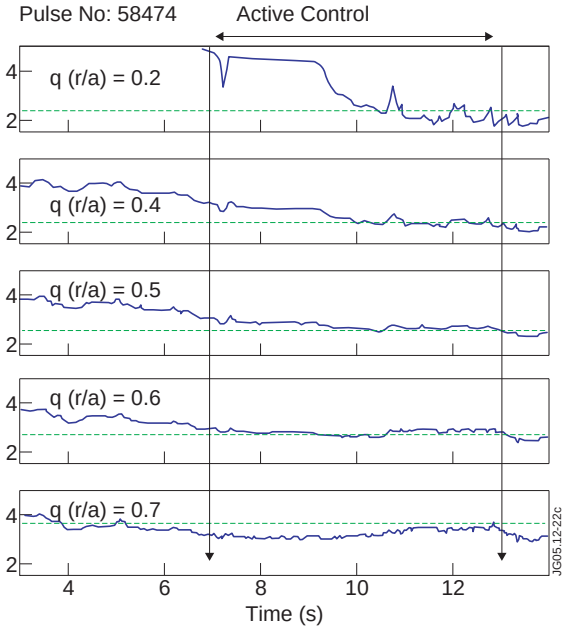

Figure 22: From Ref. 67. A typical example of Multiple Input-Multiple Output feedback control of the q-profile. Time traces are shown of the safety factor at the five radii selected for the real-time experiment with LHCD, NBI and ICRH as actuators. The setpoint values are indicated with dashed lines. The desired setpoints for q(x) (where x = r/a; see sidebar S5) at the five selected radii, x = [0.2, 0.4, 0.5, 0.6, 0.8] were q = [2.35, 2.34, 2.44, 2.69, 3.5] and the control was applied between t= 7s and t= 13s. The q-profile had a strong reversed-shear shape at the time when the control started. It then converged slowly towards the closest profile to the one requested that was achievable with the given actuators. A transient undershoot occurred between t ≈ 10s and t ≈ 11s and a minimum of the mean square error was reached at t ≈ 12s.

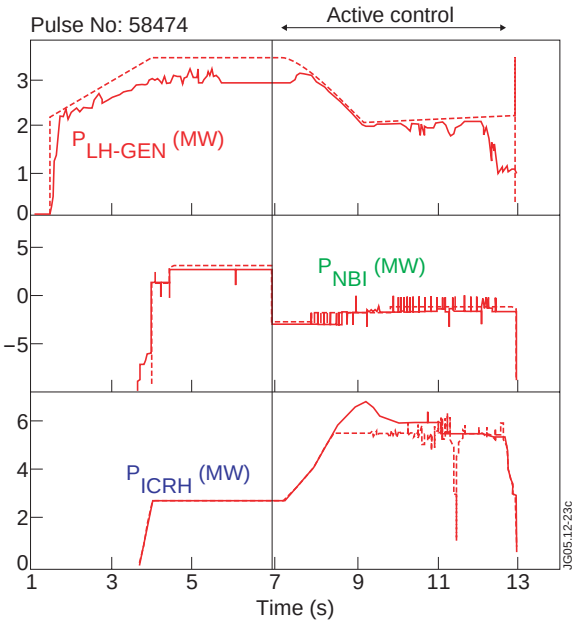

Figure 23: From Ref.67. Time evolution of the requested (dashed traces) and delivered (solid traces) LHCD, NBI and ICRH powers during the real-time control experiment shown in Fig.20. The control was applied between t= 7s and t= 13s, with initial powers at the star t of the control phase of 2.5MW for LHCD, 7MW for NBI and 3MW for ICRH. The powers requested by the controller stayed within the bounds normally allowed by the heating systems. (Here the ICRH power was mistakenly limited to 6MW, but the power requested by the real-time controller was not significantly larger than that.)

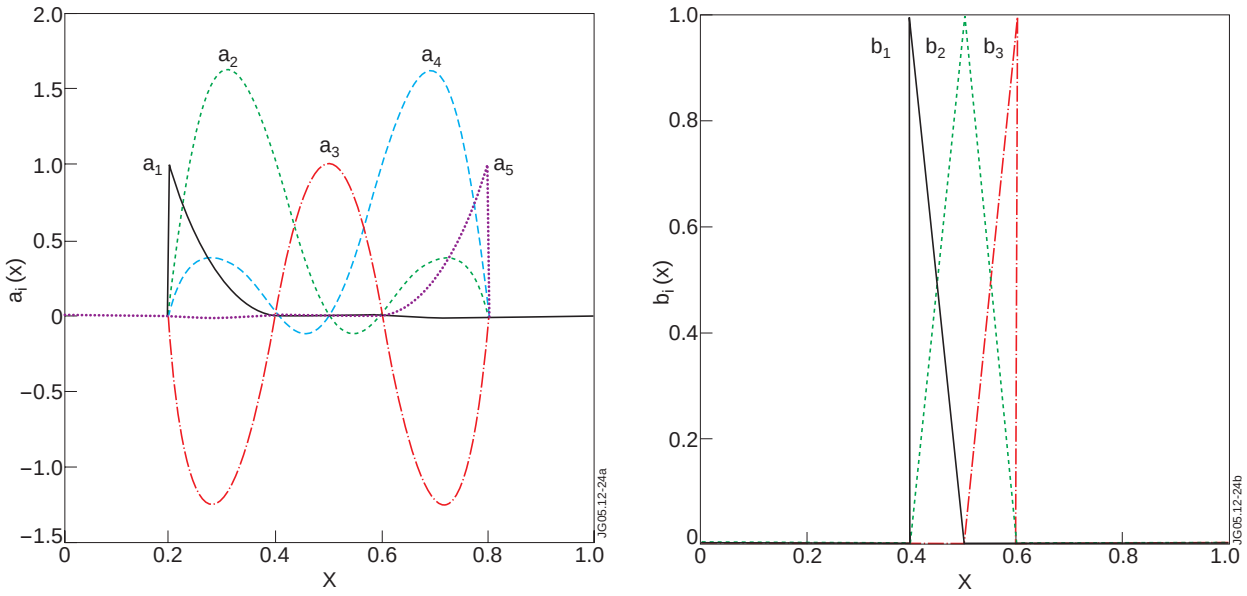

Figure 24: From Ref. 68. Basis functions used for the Galerkin projection of $\rho^*_{T_e}$ profiles (right) and i-profiles (left). (a) Five cubic splines with knots at x = [0.2, 0.4, 0.5, 0.6, 0.8] have been used to approximate the ι-profiles. (b) Three triangle functions centered at x = [0.4, 0.5, 0.6] have been used to approximate the $\rho^*_{T_e}$ profiles by a piecewise linear function in a reduced domain between x = 0.4 and x = 0.6 where the ITB is requested and controlled.

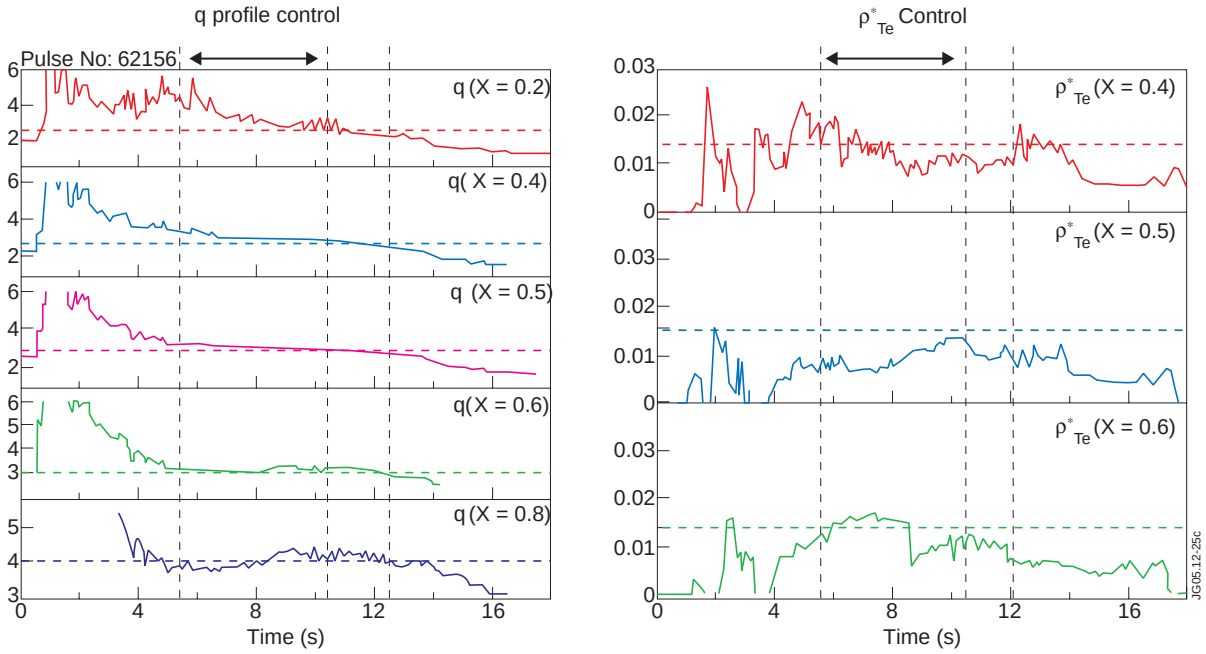

Figure 25: From Ref.68. A typical example of simultaneous (MIMO) distributed-parameter control of q and $\rho^*_{T_e}$. Time traces of the Galerkin coefficients defining the q-profile (left) and the $\rho^*_{T_e}$ profile (right) during a real-time experiment with LHCD, NBI and ICRH as actuators for controlling simultaneously the q and $\rho^*_{T_e}$ profiles. The corresponding setpoint values are indicated with dashed lines. The control was active between t = 5.5s and t = 10.25s. The requested q-profile was monotonic (sidebar S20). The target profiles are satisfactorily reached at the end of the control phase despite a strong disturbance causing a perturbation on $\rho^*_{T_e}(x = 0.6)$ at $t \approx 8.5s$.

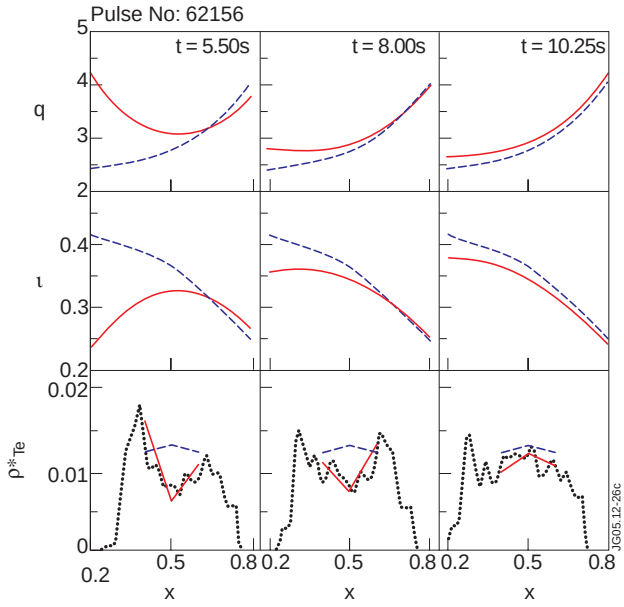

Figure 26: From Ref.68. Plots of the requested and achieved profiles during the control time window for the Pulse No: 62156. Measured profiles (solid) and target profiles (dashed) for q, ι = 1/q and $\rho^*_{T_e}$ after projection onto the span of the basis functions $(\{a_i\}^{n_a}_{i=1}$ for ι and $\{b_i\}^{n_b}_{i=1}$ for $\rho^*_{T_e}$). For $\rho^*_{T_e}$, the measured profile before projection has also been plotted (dotted). Each column corresponds to one time, respectively t = 5.5s (start of control), t = 8s, and t = 10.25s (end of control).

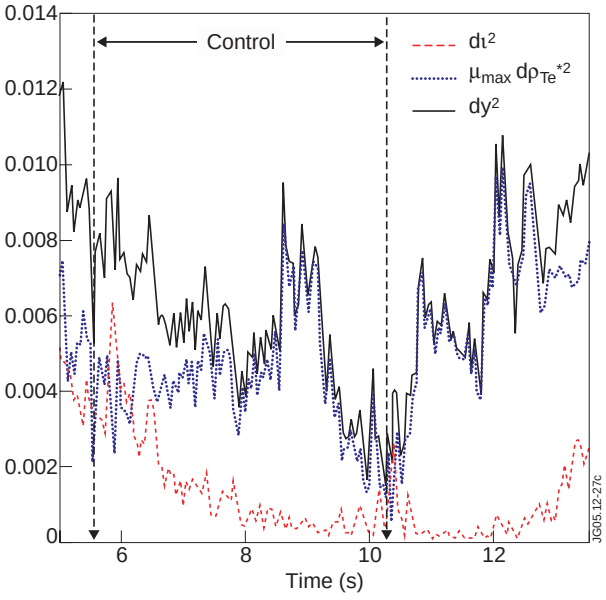

Figure 27: From Ref.68. Time evolution of the squared distance between the target and the measured profiles for ι {dashed, $d_\iota^2 = \int_{0.2}^{0.8}[\iota_{meas}(x, t) - \iota_{target}(x)]dx$}, and $\rho^*_{T_e}$ {dotted, $\rho^*_{T_e}2 = \int_{0.4}^{0.6}[\rho^*_{T_emeas}(x, t) - \rho^*_{T_etarget(x)}]dx$}, and of the global quadratic distance to be minimized (solid, $dy^2 = dt^2 + \mu_{max}\, d\,\rho^*_{T_e}{}^2$). The controller minimizes the quadratic expression defined as the global distance between the target and the measured profiles. The effect of the controller is particularly clear when looking at the evolution of the various traces after t = 10.25s when the controller action stopped because the ICRH system could not deliver the requested power. A large increase of the global distance to the target (solid) can be observed and leads to the loss of the ITB.

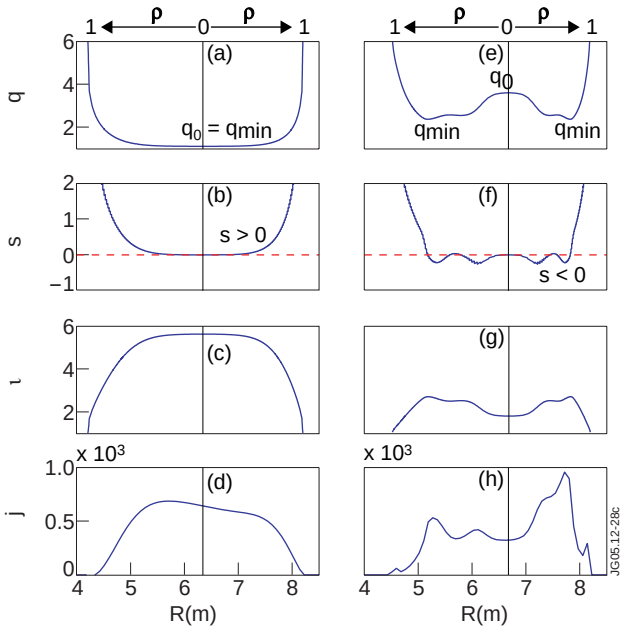

Figure A-1: Examples of monotonic and reverse shear plasmas. Plots (a) through (d) represent the same plasma having a monotonic q-profile (in which q is monotonically increasing on $0 \leq \rho \leq 1$). Plots (e) through (h) represent the same reverse shear plasma. (The normalized radius $x = r/a$ (sidebar S5), although not identical to ρ, may be substituted for ρ everywhere in this figure and its description.) The vertical line in each plot indicates the radial location of the plasma magnetic axis ($\rho = 0$; see Fig.14 of Introduction). A monotonic q profile (a) achieves its minimum value q_{min} at the magnetic axis $\rho = 0$ and is monotonically increasing in $0 \leq \rho \leq 1$. A reverse shear q profile (e) achieves its minimum value at $\rho \neq 0$, away from the magnetic axis. In either case, the value of q at the magnetic axis is denoted by $q_0 = q(\rho = 0)$. (b) The sign of the magnetic shear s for a monotonic q-profile is positive for all $0 \leq \rho \leq 1$. (f) A reverse shear plasma is one in which $s < 0$ for some set of values of ρ between 0 and 1. In particular, $s < 0$ near the magnetic axis, hence the name negative central shear. *The quantity iota $\iota = 2\pi/q$ is shown in plots (c) and (g). The current profile [(d),(h)] is not a function of the normalized flux coordinate ρ, and so does not exhibit the same symmetry with respect to magnetic axis as the other quantities. The portion of the curve to the right of the magnetic axis in plots of q, s, and ι appears compressed. This is because the plasma flux contours (see Fig.14 of Introduction) are always spaced more closely near the outside of the torus, hence the radial dimension corresponding to the normalized flux $0 \leq \rho \leq 1$ must be smaller on that side of the magnetic axis.*